Boosting the electrocatalytic activity of NiSe by introducing MnCo as an efficient heterostructured electrocatalyst for large-current-density alkaline seawater splitting

Reza Andaveh [a], Alireza Sabour Rouhaghdam [a], Jianping Ai [b], Meysam Maleki [a], Kun Wang [b], Abdolvahab Seif [c], Ghasem Barati Darband [d,*], Jinyang Li [b,e,**]

[a] Department of Materials Engineering, Faculty of Engineering, Tarbiat Modares University, P.O. Box 14115-143, Tehran, Iran
[b] Key Laboratory of Advanced Technologies of Materials (Ministry of Education), School of Materials Science and Engineering, Southwest Jiaotong University, Chengdu 610031, China
[c] Dipartimento di Fisica e Astronomia "G. Galilei", Università di Padova, via Marzolo 8, I-35131 Padova, Italy
[d] Materials and Metallurgical Engineering Department, Faculty of Engineering, Ferdowsi University of Mashhad, Mashhad 91775-1111, Iran
[e] Yibin Institute of Southwest Jiaotong University, Yibin 644000, China

ARTICLE INFO

ABSTRACT

Hydrogen production employing seawater electrolysis is a sustainable strategy for future energy prospects. This study reports high-performance bifunctional water (seawater) electrocatalyst by designing 3-D heterostructured MnCo/NiSe/NF. MnCo/NiSe is concurrently highly energetic toward HER (22.1, 182.8, and 211.6 mV in alkaline water and 31.4, 216.3, and 270.1 mV in alkaline seawater to touch current densities of -10, -500, and -1000 mA cm^{-2}, respectively) and OER (225.8, 340.4, and 370.7 in alkaline water and 261.3, 419.4, and 460.2 mV in alkaline seawater to attain 10, 500, and 1000 mA cm^{-2}, respectively). Interestingly, with cell voltages of 1.41, 1.67, 1.88, and 1.92 V in 1.0 M KOH and 1.44. 1.82, 1.99, and 2.11 V in 1.0 M KOH + seawater to run 10, 100, 500, and 1000 mA cm^{-2}, respectively. DFT based modeling rationalizes our experiments and indicates the synergistic effects between MnCo and NiSe in their complex.

1. Introduction

The limitations of non-renewable conventional energy sources, such as oil and natural gas, and their environmental consequences have boosted the demand for clean energy generated from renewable sources (wind, solar, etc.) [1]. Hydrogen is considered an excellent substitute for traditional fossil fuels as a clean and high-density energy carrier [2]. There are various strategies for producing hydrogen; one of the cleanest methods for producing highly pure H$_2$ on a wide scale without any carbon-based emissions is electrochemical water electrolysis powered by electricity produced from renewable sources [3]. Seawater electrolysis has several key advantages over freshwater electrolysis, which has been the subject of extensive research. These advantages include seawater's abundance and sustainability, ease of integration with emerging ocean technologies, collaboration in the production of safe drinking water, and the ability of its dissolved salts for promoting the ionic conductivity [4]; All of these together have led to increasing research attention to it. For seawater electrolysis to be an efficient and economical method of hydrogen production, highly active electrocatalysts made of non-precious metals are required for hydrogen evolution reaction (HER) and the oxygen evolution reaction (OER). Especially it is expected that an electrocatalyst withstands severe industrial conditions and displays stable performance at extremely high current densities (i.e., possessing low overpotentials and showing highly stable performance in current densities more than 500 and 1000 mA cm^{-2}) before it gets used in actual industrial conditions [5].

Although seawater electrolysis is a sustainable approach for producing hydrogen, several vital challenges exist in developing high-efficiency electrocatalysts for HER and OER. In seawater, the primary obstacle to HER performance is related to the presence of indissoluble

---

species, such as impurities and bio-organisms or created by the reaction of the alkali ions with the conductive substance OH⁻ (Calcium hydroxide, magnesium hydroxide, etc.). These precipitates will cover the active sites of electrocatalysts and lowering their electrocatalytic efficiency [6]. Regarding the OER, the nature of the four-electron OER process unavoidably prompts an energy barrier that decreases seawater electrolysis efficiency [7]. Besides that, one of the issues with seawater is that large overpotentials must be used to attain high current densities owing to the presence of chloride anions (Cl⁻ ~ 0.5 M). In this scenario, chloride ions interfere with the OER to create hypochlorite (ClO⁻), resulting in a significant reduction in water electrolysis efficiency [8]. Hypochlorite and chlorine result from the chlorine evolution reaction (CER) that can surpass OER, thus hampering HER and corroding the electrodes [6,9]. Concerning the CER, in the alkaline electrolyte, the chlorine will react with OH⁻ to create hypochlorite, which has a 490 mV higher onset potential than the OER. As a result, it is required for advanced OER electrocatalysts to have high-efficiency performance at overpotentials below 490 in order to prevent the production of hypochlorite [10].

In recent decades, high-noble metal electrocatalysts (Pt, Ir, Ru, Rh) have been utilized for improving HER and OER. However, due to their limited resources and high prices, they are not widely used [11]. Due to their excellent performance, great stability, and cheap cost, abundant earth transition metal chalcogenides (Co, Fe, Ni, Mo, etc.) have recently come to be recognized as superior electrocatalysts for water electrolysis [12]. Amongst them, Selenide-based materials have recently attracted attention as a suitable group for energy proposes due to their decent properties in comparison with their "star chalcogenide" sulfides corresponding [13]. Since the 3d orbital of Se has an energy level near the 3 s and 3p orbitals of metals, it may contribute to bonding with metal atoms. Such an electron arrangement causes transition metal selenides to become even more metallic, which is advantageous for electron transport [14]. Besides, transition metal selenides also benefit from simple preparation, good stability, and higher electrocatalytic performance, making them an ideal choice for electrocatalytic reactions. Nickel selenides are considered decent water electrolysis electrocatalysts owing to their abundant reserve, economical, and acceptable conductivity [15]. Since nickel and Selenide have small electronegativity differences as well as the specific electronic structure of nickel ($3d^8$ $4s^2$), the two can produce various stoichiometric mixtures [16]. However, similar to other transition metal chalcogenides, nickel-based selenides struggle with the difficulty between improved activity and poor conductivity in nanosized particles and good conductivity with poor electrocatalytic performance in bulk [17]. So, as mentioned, nickel-selenide-based electrocatalysts for HER and OER are an excellent alternative to costly metal electrodes, but their performances need to be improved.

Manganese (Mn) and cobalt (Co) are two elements that have been shown to have a significant effect on improving catalytic properties [18]. Manganese is also one of the elements that have been shown to have a significant effect on increasing electrocatalytic activity, electrochemical surface area (ECSA), and electrocatalytic stability [19]. For example, in a recent study by our group [20], it was clear that when Mn was incorporated into the NiSe structure, it modified and optimized the morphology and increased the amount of ECSA, consequently improving the HER, OER, and urea oxidation reaction (UOR) performance. The prepared Ni-Mn-Se could significantly decrease HER overpotential from 122 to 28 mV at $-$ 10 mA cm^{-2}. Various cobalt and manganese base compounds have been synthesized for HER and OER; nevertheless, further improvements are needed to industrialize these electrodes. In addition, the use of the easy, cheap and fast method is also one of the critical factors for the development of hydrogen production technology from water electrolysis. It is noteworthy that till now, relatively little comparative research has been done on the efficiency in seawater and freshwater of electrocatalysts.

In this work, we developed a bifunctional MnCo/NiSe

heterostructure electrocatalyst via a simple two-step electrodeposition procedure to overcome the challenges of synthesizing high-efficiency electrocatalysts in extreme conditions. The MnCo/NiSe showed excellent catalytic performance towards OER and HER in alkaline water (1.0 M KOH) and alkaline seawater (1.0 M KOH + seawater). The coupling of MnCo to NiSe results in outstanding improvements such as enhanced conductivity, larger ECSA, boosted conductivity, and increased turnover frequency (TOF). Besides, due to the unique 3-D morphology of microspheres containing interconnected nanosheets, MnCo/NiSe displayed superaerophobicity/superhydrophilicity features, which can significantly improve catalytic stability and mass transfer in high current densities. Furthermore, MnCo/NiSe electrocatalyst possessed super-low HER and OER overpotentials in basic water and seawater. For surpassing $-$ 10, $-$ 500, and $-$ 1000 mA cm^{-2} it only needed overpotentials of 22.1, 182.8, and 211.6 mV in alkaline water and 31.4, 216.3, and 270.1 mV in alkaline seawater for HER, respectively, and for OER, MnCo/NiSe for attaining current densities of 10, 500, and 1000 mA cm^{-2} required only overpotentials of 225.8, 340.4, and 370.7 in 1.0 M KOH and 261.3, 419.4, and 460.2 mV in 1.0 M KOH + seawater, respectively. It also could withstand 150 h of non-stop operation at a high current density of 500 mA cm^{-2} in 1.0 M KOH + seawater without creating any hypochlorite. The MnCo/NiSe || MnCo/NiSe electrolyzer system also exhibited low cell voltages of 1.41, 1.67, 1.88, and 1.92 V in alkaline water and 1.44. 1.82, 1.99, and 2.11 V in alkaline seawater for running 10, 100, 500, and 1000 mA cm^{-2}, respectively, with superb Faradaic efficiency and long-standing catalytic durability. Overall, this research exhibits a novel approach for designing and preparing prospective electrocatalysts for economical seawater electrolysis.

2. Experimental section

2.1. Preparation of electrocatalysts

2.1.1. Preparation of NiSe/NF

For preparation of the NiSe electrocatalysts, a potentiostatic electrodeposition method was employed. The substrate utilized for electrodeposition of all electrocatalysts was nickel foam (NF) with a size of 1 × 1 cm^{-2}. Before the synthesis procedure, NFs were cleaned in ethanol and immersed in 20% hydrochloric acid for 15 min and 25 s, respectively. To synthesize of NiSe electrocatalyst, the bath of electrodeposition consisted of 0.057 M NiCl$_2$0.6 H$_2$O (Ni ion source), 0.01 M SeO$_2$ (Se ion source), 0.2 M LiCl (conductivity booster), and 0.03 M CaCl$_2$. A three-electrode setup in ambient temperature was chosen for the first step of electrodeposition, in which Ag/AgCl and graphite electrodes serve as a reference and counter electrodes, respectively. A constant potential of $-$ 1.15 V vs. Ag/AgCl for electrodeposition of NiSe electrodes was obtained by taking a CV test, and the synthesis time was 15 min

2.1.2. Synthesis of the MnCo/NiSe/NF

In the next step, MnCo was electrodeposited on NiSe as-prepared samples by the Cyclic voltammetry (CV) method. To synthesize of MnCo/NiSe electrocatalyst, the bath of electrodeposition consisted of 0.01 M MnCl$_2$0.4 H$_2$O and 0.01 M CoCl$_2$0.4 H$_2$O. An Ag/AgCl and a graphite electrodes were employed as reference and counter electrodes, and the as-synthetized NiSe/NF samples were used as the working electrode. MnCo layer was deposited on the NiSe/Ni foam samples at the potential range of $-$ 0.2 to -1.32 V vs. Ag/AgCl. Moreover, a constant value of 20 mV s^{-1} was used as scan rate. For optimization of the number of cycles, the scan rate was set at a constant value, and the number of cycles varied from 2 to 15 (2, 5, 10, 15). All synthesis material used in this work provided by Merck Co.

2.2. Chemical and structural characterization

To explore the morphology of samples, a field emission scanning

electron microscopy (FESEM, TESCAN MIRA3) and transmission electron microscope (TEM and HRTEM, JEOL JEM-2100) were employed. An energy-dispersive X-ray spectroscope (EDS) and scanning transmission electron Microscope (STEM) were utilized to investigate the elemental mapping and compositions. X-ray diffraction (XRD) (X'Pert MPD, Cu Kα radiation ($\lambda = 1.54178$ Å)) and X-ray photoelectron spectroscopy (Thermo-Scientific ESCALAB 250Xi) was also utilized to study the phase structure and surface chemistry of specimens. BL11B beamlines at Shanghai Synchrotron Radiation Facility (SSRF) (Shanghai, China) were used to perform K-edge analysis with Si(111) crystal monochromators. The XAFS spectra were recorded at room temperature using a 4-channel Silicon Drift Detector (SDD) Bruker 5040. Samples were pressed into thin sheets 1 cm in diameter and sealed with Kapton tape film prior to analysis at the beamline.

2.3. Electrochemical characterization

For all the electrochemical evaluations, an SP-300 Bio-Logic potentiostat was used with a typical three-electrode system. In this setup, graphite and Ag/AgCl served as the counter and reference electrodes. For the electrolytes, 1.0 M KOH and 1.0 M KOH + Seawater (obtained from Persian Gulf (pH = 7.7)) were employed, and the fabricated electrocatalysts were used as working electrodes. For electrocatalytic evaluation of different electrodes, Linear Sweep Voltammetry results were recorded with a sweep rate of 5.0 mV s^{-1} and corrected for iR drop (by 100%) taking the uncompensated resistance (R_u) of from electrochemical impedance measurements (EIS). Additionally, to investigate the HER kinetics, the Tafel slopes are originated from LSV curves. For further analysis of HER kinetic, the EIS under a frequency range of 100 kHz to 100 mHz was also performed in a constant potential of -1.1 V vs. Ag/AgCl. For calculating the double-layer capacitance (C_{dl}) of different electrocatalysts, CV curves were obtained at scanning rates of 20–120 mV s^{-1}. For assessing the stability performance of MnCo/NiSe electrocatalyst towards HER, OER, and cell, chronopotentiometry and multistep chronopotentiometry tests were executed under an anodic (OER, cell) and cathodic (HER) current density of 500 and 10–250 mA cm^{-2} (15 min for each step) for 200 h in alkaline seawater electrolyte, respectively. Furthermore, the durability ability of MnCo/NiSe electrocatalyst was tested after 3000 and 5000 CVs at a potential range of 0 to -0.2 V with a scan rate of 100 mV s^{-1}. To evaluate the gas bubble detachment behavior of MnCo/NiSe, dynamic specific resistance test at an overpotential of -400 mV and a frequency of 10 kHz was performed during the 240 s. The oxygen and hydrogen gas were spotted by Gas Chromatography (Bruker GC450). The Gas Chromatography directly coupled to the MnCo/NiSe || MnCoNiSe cell via gas tubes. When the i-t quantities were obtained at 50 mA cm^{-2} the generated gas was noted at every 10 min. Therefore, the Faradaic efficiency can be calculated as mentioned below:

$$FE_{O2} = \frac{4 \times 96485 \times n_{o2}}{Q_{OER}} \quad (1)$$

$$n_{O2} = \frac{V_{o2}}{Vm} \quad (2)$$

$$FE_{H2} = \frac{2 \times 96485 \times n_{H2}}{Q_{HER}} \quad (3)$$

$$n_{H2} = \frac{V_{H2}}{Vm} \quad (4)$$

In which, V is volume of generated gas attained by Gas Chromatography, V_m is molar volume 22.4 L mol^{-1}, the n is molar mass of generated gas, and Q the total charge distributed in electrocatalyst.

All the reported potentials in this research are reported based on the reversible hydrogen electrode (RHE) using the formula below.

$$V_{RHE} = V \text{ (vs. Ag/AgCl)} + V° \text{ Ag/AgCl} + 0.059 \text{ pH} \quad (5)$$

2.4. Calculation of double-layer capacitance (C_{dl}), roughness factor (RF), and electrochemical surface area (ECSA)

CV curves were utilized to calculate the C_{dl} of different electrodes. Hence, CV test were performed at a range of scan rate from 20 to 120 mV s^{-1} in non-faradic potentials region (-0.85 to -0.95 V vs. Ag/AgCl for MnCo/NiSe, -0.67 to -0.77 V vs. Ag/AgCl for NiSe). The C_{dl} values were calculated through the linear relationship between the subtraction of the cathodic and anodic current densities ($J_{anodic} - J_{cathodic}$) with different scan rates. The ECSA values were calculated according to the formula below:

$$ECSA = \frac{C_{dl}}{C_s} \quad (6)$$

where C_s is the flat surface capacitance (40 μF cm^{-2}). The Eq. (7) was applied to calculate the RF value:

$$RF = \frac{C_{dl}}{C_0} \quad (7)$$

where C_0 is the capacitance of ideal planar metal oxides (i.e., NiO) with smooth surfaces (60 μF cm^{-2}).

2.5. Calculation of turnover frequency (TOF)

TOF figures can be attained from the geometrical substrate surface area and current density at a set overpotential throughout the HER, according the formula (8):

$$TOF = \frac{\text{Total Hydrogen Turn } Overs/\text{cm}^2\text{geometric } area}{\text{Surface active } sites/\text{cm}^2\text{geometric } area} \quad (8)$$

All number of evolved hydrogen bubbles can be extracted according to the current density at a set overpotential, based on the Eq. (9):

$$H_2 = (j\frac{mA}{cm^2})(\frac{1C\ s^{-1}}{1000mA})(\frac{1mol\ e^-}{96485.3C})(\frac{1molH_2}{2mol\ e^-}) \times (\frac{6.022 \times 10^{23}H_2 molecules}{1molH_2})$$

$$= 3.12 \times 10^{15}\frac{H_2}{s} \text{ per } \frac{mA}{cm^2} \quad (9)$$

Supposing that all of the catalytic centers at the surface are participate in the HER, the number of active surface sites can be calculated as follows:

$$N = (\frac{4atoms}{43.76A})^{\frac{2}{3}} = 9.01 \times 10^{14} atoms.cm^{-2}_{real} \quad (10)$$

Then, the TOF value at each current density can be measured by the Eq. (11):

$$TOF = (\frac{3.12 \times 10^{15}\frac{H_2/s}{cm^2} \text{ per } \frac{mA}{cm^2} \times |j|}{(9.01 \times 10^{14} atoms.cm^{-2}_{real}) * A_{ECSA}}) \quad (11)$$

2.6. DFT calculations detail

Our periodic DFT analysis was carried out by spin-polarized calculations using the Projector Augmented Wave (PAW) method, for the electronic-ion interaction, implemented in the Vienna Ab initio Simulation Package (VASP) for the electronic-ion interaction [21]. Also, Perdew-Burke-Ernzerhof (PBE) [22] form generalized gradient approximation (GGA) was used for the exchange-correlation potential. The DFT-D3 method within the Grimme's correction [23] was applied in all calculations to consider the van der Waals forces. A cutoff energy of 450 eV was set to expand the plane waves as the basis set. Considering our surface energy calculations [24], the modeled heterojunction is

composed of (002) crystal faces of NiSe and (111) crystal faces of MnCo with a minimum mismatch between the two structures. Calculations were done using the Monkhorst−Pack method and a $(3 \times 3 \times 1)$ centered k-point grid. The energies and forces were calculated until they converged to within 10^{-5} eV and 0.03 eV $\mathring{A}^{-1}$ respectively.

3. Results and discussion

3.1. Characterization of as-prepared electrocatalysts

As the preparation route is graphically demonstrated in Fig. 1, the MnCo/NiSe electrocatalyst was synthesized via an easy two-step electrodeposition procedure, which is considered a fast, simple, and cost-saving approach and causes 3-D nanostructures directly developed on conductive substrates. In step 1, the NiSe sublayer was synthesized with the potentiostatic method at a constant voltage and time on a Ni foam substrate. In step 2, to determine the effect of the number of cycles parameter on the morphology by applying the cyclic voltammetry (CV) method in different cycles (2, 5, 10, and 15), the optimized MnCo coating was electrodeposited on as-prepared NiSe samples.

Field emission scanning electron microscopy (FESEM) employed to analyze the morphology of the as-fabricated electrocatalysts. FESEM images of NiSe are shown in Fig. 2a-d. As it is clear, the NiSe surface has an almost smooth morphology, which could result in poor electrocatalytic performance due to its low exposed catalytic surface area. Figs. S2 and 1e-h are the FESEM images of MnCo/NiSe in cycles of 2, 5, 15, and the optimized cycles of 10, respectively. As can be seen, in the 10-cycle optimization sample, the unique 3-D morphology of microspheres (with an average diameter of 1.1 μm) containing interconnected nanosheets (with an average thickness of 24.0 nm) can be observed. Such a highly open and interconnected network could significantly promote electrolyte accessibility and accelerate electron transport. Therefore, it can be concluded that the addition of the MnCo layer has a positive effect on optimizing and roughening the morphology. Nevertheless, as shown in Fig. S2a-b, the samples prepared in cycles 2 and 5, compared to the sample prepared in 10 cycles, although the microspheres can be detected, the nanosheets did not have the opportunity to form due to fewer cycles. In the sample prepared in 15 cycles, although the microspheres can still be seen, the large number of cycles caused the nanosheets inside the microspheres to become thicker and smoother and the microspheres to fill, which eventually caused decreasing ECSA, which was also confirmed by electrochemical measurements (Optimization procedure is mentioned in Supplementary Data). Furthermore, the effect of adding the second layer of MnCo to the NiSe sublayer on the electrocatalytic properties will be discussed in the electrochemical analysis section. The transmission electron microscope (TEM) and high-resolution transmission electron microscopy (HRTEM) are utilized to

further characterize NiSe and MnCo/NiSe samples. As evident from TEM images of MnCo/NiSe (Fig. 2i-k), a microsphere containing interconnected nanosheets can be identified, which are in line with FESEM images of MnCo/NiSe (Fig. 2e-h).

Moreover, in Fig. 2i-k, two areas, dark and light, can be distinguished, which can be evidence of the successful formation of MnCo nanostructure on NiSe substrate, respectively. In Fig. 2k, the interface of these two structures can be seen, unlike NiSe, where only one single-phase NiSe region is detectable (Fig. S2a-d). The darker and lighter area in Fig. 2k could be attributed to MnCo and NiSe, respectively. The interface between the MnCo and NiSe phases and their crystalline features can also be detected through the HRTEM image (Fig. 2h). According to HRTEM results (Fig. 2l), the interplanar distance to the lattice fringes is 0.183 nm and 0.192 nm, which is ascribed to the (110) surface of NiSe and (111) surface of the Co in MnCo structure. Furthermore, the homogenous dispersion of Mn, Co, Ni, and Se particles on Ni foam substrate in the MnCo/NiSe electrode was successfully detected by the energy dispersive spectroscopy (EDS) coupled with scanning TEM (STEM-EDS) (Fig. 2n). Besides, the FESEM-EDS analysis also proves the uniform dispersion of Mn, Co, Ni, and Se in the MnCo/NiSe electrode (Fig. S3) and Ni and Se in the NiSe sample (Fig. S1e-g) and evaluates that the normalized atomic ratio of Co:Ni:Se:Mn and Ni:Se are 1:0.45:0.12:0.03 and 1:0.5, respectively. Fig. S2a-c and Fig. S3 also show FESEM images and the atomic percentages of Mn, Co, Ni, and Se elements obtained from the FESEM-EDS analysis in the MnCo/NiSe samples prepared in cycles 2, 5, 15, and 10, which also verifies the presence of all as-mentioned elements in MnCo/NiSe electrode. Needless to say, as the number of cycles increased to 15, the atomic percentages of Mn and Co increased to about 3% and 64%.

Powder X-ray diffraction (XRD) was employed to investigate the phase structure of the MnCo/NiSe and NiSe electrodes (Fig. S4). As demonstrated in Fig. S4, in the XRD patterns of both MnCo/NiSe and NiSe, there are three individual sharp XRD diffraction peaks located at 44.5°, 51.9°, and 76.4°, which, respectively, were related to the (111), (200), and (220) planes of Ni substrate (00–004–0850) [25]. In the XRD pattern of the NiSe sample, the four diffraction peaks are clearly seen at the 2θ positions of 32.84°, 33.60°, 49.78°, and 59.60°, which are in perfect agreement with the (101), (002), (110), and (102) planes of NiSe (01−075−610) [26]. Noticeably, the peak arising at 44.51° could be attributed to the metallic nickel and NiSe, which shows the preferential growth of NiSe on metallic Ni substrate during the electrodeposition process. The peaks associated with the NiSe phase can still be identified in the XRD pattern of the MnCo/NiSe electrocatalyst. There are also some detectable shifts and intensity changes of the related peaks in the XRD pattern of MnCo/NiSe relative to the XRD pattern of NiSe as specified. As can be seen, the peaks associated with Ni substrate and Co at the 2θ positions of 45.92° (111), 53.54° (200), and 79.14° (220)
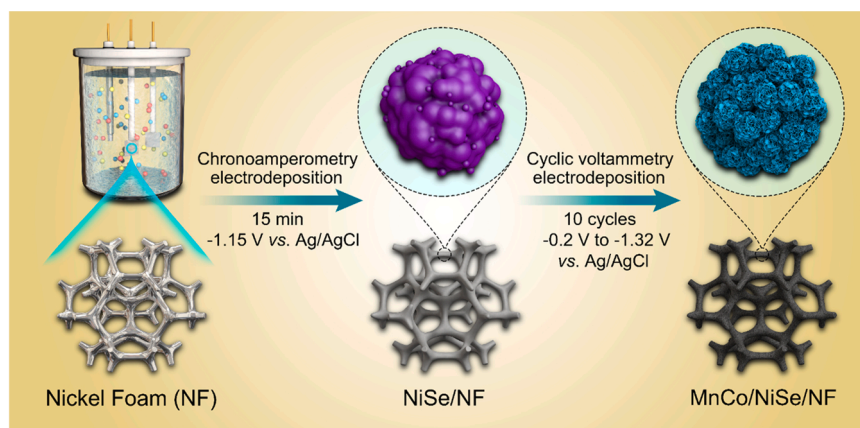

Fig. 1. Schematic of the preparation of MnCo/NiSe and NiSe electrocatalysts.
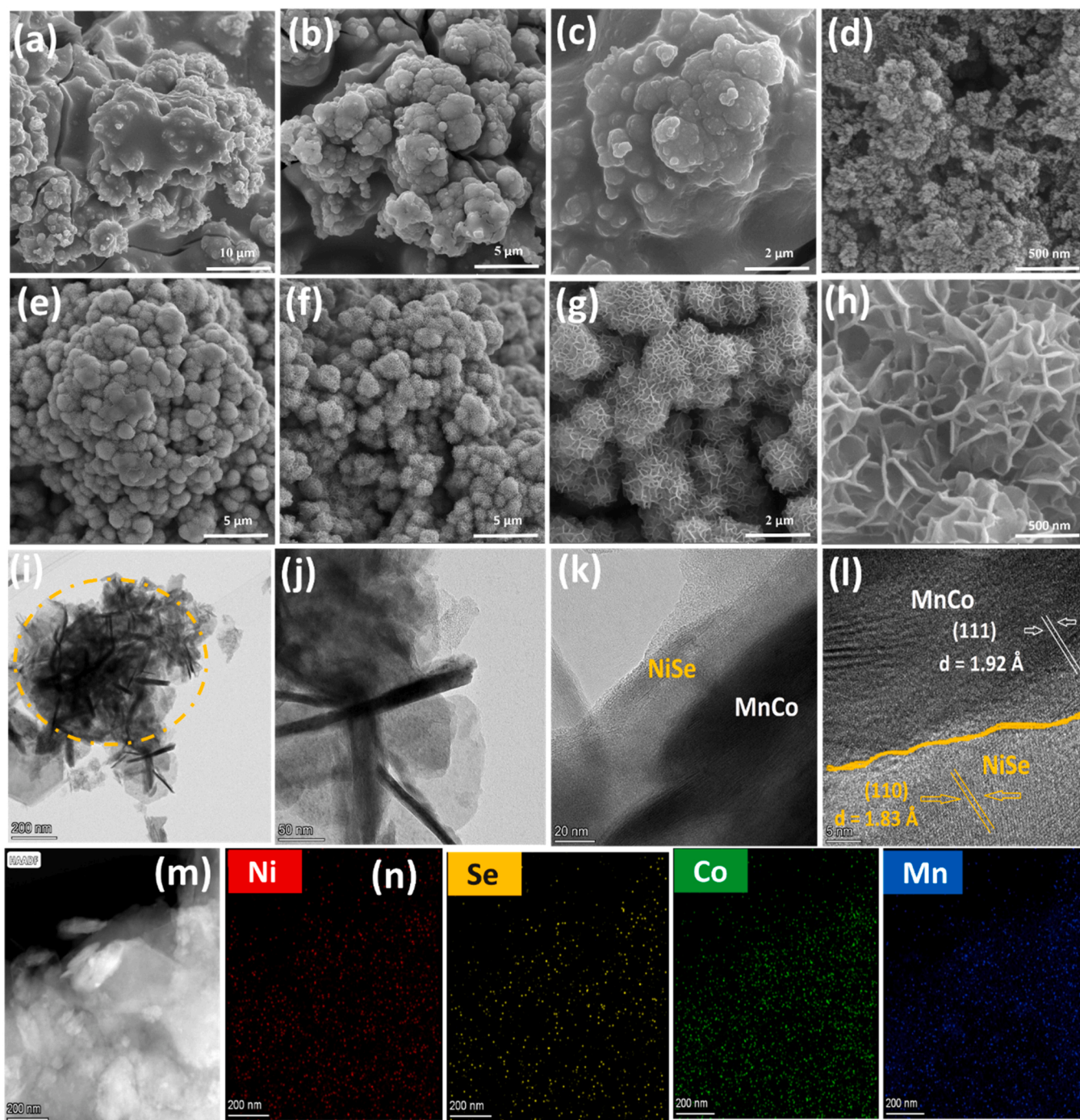
Fig. 2. Low and high magnification FE-SEM images of NiSe electrode (a-d); Low and high magnification FE-SEM images of MnCo/NiSe electrocatalyst (e-h); TEM (i-k) and HRTEM images (l) of MnCo/NiSe electrode; (m) HAADF and (n) STEM-elemental mapping of MnCo/NiSe electrode indicating the uniform dispersion of Ni (red), Se (yellow), Co (green), and Mn (blue).

(00−015−806) are overlapped [27]. It should be noted that Mn has not shown a peak due to the low atomic percentage, the small number of electrodeposition cycles, and the low thickness of the deposited layer.

For determining the composition and electronic states of different elements in MnCo/NiSe and NiSe electrocatalysts X-ray photoelectron spectroscopy (XPS) was used. Fig. S5 indicates the peaks related to Ni, Se, Co, and Mn in the MnCo/NiSe electrode. The presence of these four elements was also confirmed through EDS and STEM data. Furthermore, the signals related to carbon and oxygen are mainly due to contamination or surface oxidation of the electrode caused by interaction with environment conditions [28]. As is displayed in Fig. 3a, the Ni $2p_{3/2}$

spectrum (for NiSe and MnCo/NiSe) displays a satellite peak located at 862.0 eV and peaks attributed to Ni^{2+} and Ni^{3+} at 855.1 and 856.2, respectively. The Ni $2p_{1/2}$ spectrum displays a main peak at 872.8 eV with two peaks attributed to Ni^{+3} and Ni^{+2} at 874.6 and 872.5 eV and a satellite peak at 880.1 eV [29]. Fig. 3b shows the Se 3d peaks of NiSe and MnCo/NiSe. The XPS spectrum of Se 3d for NiSe is comprises two peaks at 53.80 eV (Se $3d_{5/2}$) and 54.45 eV (Se $3d_{3/2}$), and the peak at 58.24 eV can be attributed to oxidized Se [30]. Noticeably, in the Ni 2p (Fig. 3a) and Se 3d (Fig. 3b) peaks of MnCo/NiSe, there is an apparent positive shift relative to NiSe, which indicates the decrease of electron densities around the Ni and Se atoms after adding Mn and Co atoms [31]. It is
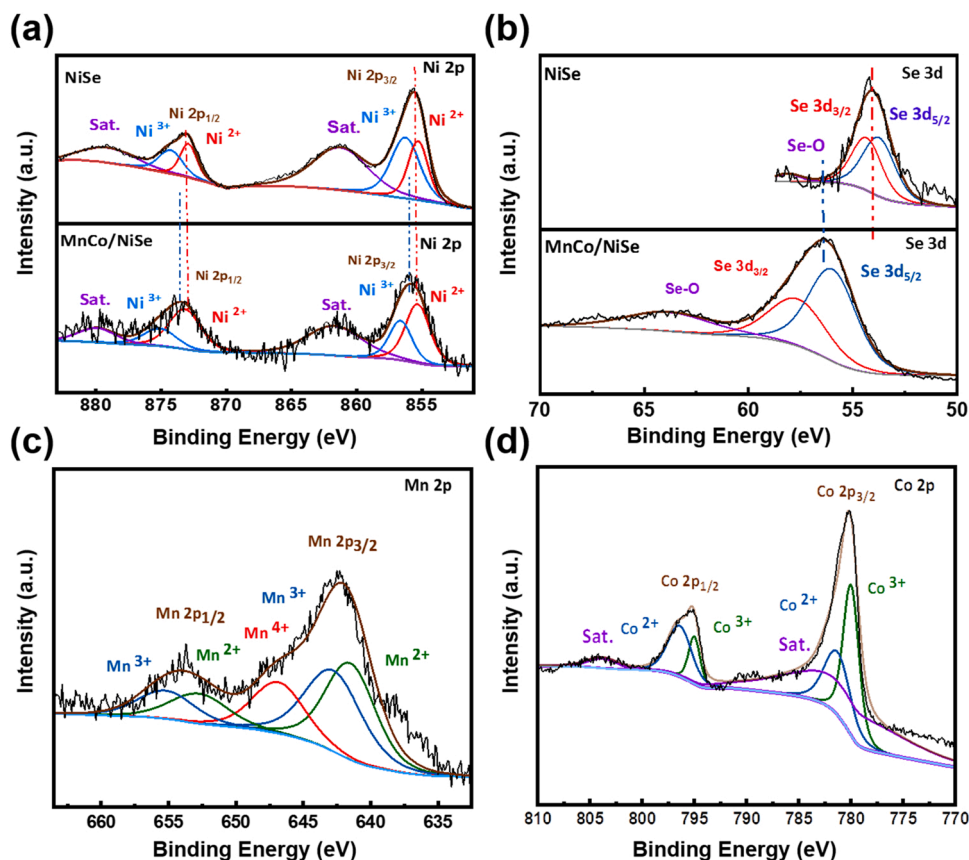
Fig. 3. (a) XPS spectrum of Ni 2p. (b) Se 3d. (c) Mn 2p. (d) Co 2p.

revealed that the presence of components with different electronegativity within the heterostructure can cause the transfer of electrons among different structure constituents, which usually is detectable by the binding energy shift in XPS spectra. It should be noted that for some heterostructures, by rearranging the electrons, the electronic configurations or the band structures of the constituents will be optimized, which is beneficial for electrocatalytic activity [32]. The Mn 2p spectrum (Fig. 3c) indicates two main peaks of $2p_{3/2}$ at 642.0 eV and $2p_{1/2}$ at 653.5 eV with a distance of 11.5 eV. The Mn 2p spectrum can be fitted to three pairs of characteristic peaks of Mn^{4+}, Mn^{3+}, and Mn^{2+} that were located at 645.5, 642.4, and 653.0 eV, and 641.0 and 651.6 eV, respectively [33]. Regarding the Co ions, four peaks were spotted in the Co 2p XPS spectra (Fig. 3d): two prominent peaks, at 778.6 and 793.2 eV, corresponding to the Co $2p_{3/2}$ and Co $2p_{1/2}$ with a distance of 15.4 eV (Fig. 3c). The presence of the Co^{2+} and Co^{3+} are confirmed. Furthermore, the XPS spectrum of Co 2p (Fig. 3d) comprises six peaks, which the peaks centered at 795.1 and 779.5 eV match Co^{3+}, and the peaks situated at 796.6 and 781.2 eV should be related to Co^{2+}. Moreover, the shakeup satellite peak attributing to Co^{3+} and Co^{2+} appears at 802.6 and 784.4 eV, respectively [34].

In the first stage, the procedure of finding the optimal sample was performed to be evaluated in further analysis (more detail is in Supplementary data).

3.2. Catalytic performance of as-prepared electrocatalysts

3.2.1. HER performance of MnCo/NiSe in alkaline seawater and freshwater

To investigate the intrinsic properties of optimized MnCo/NiSe electrocatalyst and the difference between its catalytic activity and NiSe, their electrocatalytic performance towards HER were investigated by a typical three-electrode setup in different electrolytes (Fig. 4). All raw data was modified through the iR correction to reveal the inherent activities of electrocatalysts. Fig. 4a shows the Linear Sweep voltammetry (LSV) curves of MnCo/NiSe, NiSe, Pt foil, and Ni foam in alkaline water and seawater with a scan rate of 5.0 mV s^{-1} for HER. It must be said that, for the sake of comparison, Pt foil was chosen because of its higher HER electrocatalytic activity rather than Pt/C [35]. As can be seen in Fig. 4a, MnCo/NiSe electrode needs ultralow overpotentials of 22.1, 120.0, 182.8, and 211.6 mV at -10, -100, -500, and -1000 mA cm^{-2}, respectively, in 1.0 M KOH for HER, which is much lower than those of NiSe (73.8 mV and 393.8 mV at -10 mA cm^{-2} and -500 mA cm^{-2}, sequentially) and Pt foil (49.5 mV and 408.4 mV at -10 mA cm^{-2} and -500 mA cm^{-2}, sequentially). In alkaline seawater electrolyte, the MnCo/NiSe electrode also displays a much better catalytic activity towards HER by having low overpotentials of 31.4, 134.3, 216.3, and 270.1 mV at -10, -100, -500, and -1000 mA cm^{-2}, sequentially, which is much less than those of NiSe (139.1 mV and 471.7 mV at -10 mA cm^{-2} and -500 mA cm^{-2}, sequentially), Pt foil (94.2 mV and 547.1 at -10 mA cm^{-2} and -500 mA cm^{-2}, sequentially), and Ni foam (220.8 mV and 693.6 mV at -10 mA cm^{-2} and -500 mA cm^{-2}, sequentially). According to the results, the addition of the MnCo layer to NiSe has been able to significantly enhance the HER efficiency of NiSe, which could be due to the synergistic effect between different structures. Additionally, selenide-based catalysts are commonly considered to have favorable HER electrocatalytic activity since the Se atoms can cause an attraction for H* intermediates and rapidly release H_2 molecules [36]. It should be noted that in both HER and OER, in almost all cases, catalytic efficiency in alkaline seawater is lower than in alkaline water, which is mostly attributed to blocking some of the surface active sites due to the presence of bacteria, impurities, and alkali cations (e.g., $Mg(OH)_2$ and $Ca(OH)_2$ in seawater). Overall, the HER performance of the MnCo/NiSe catalyst was superior to those of the newly investigated HER electrocatalysts (Table S1).
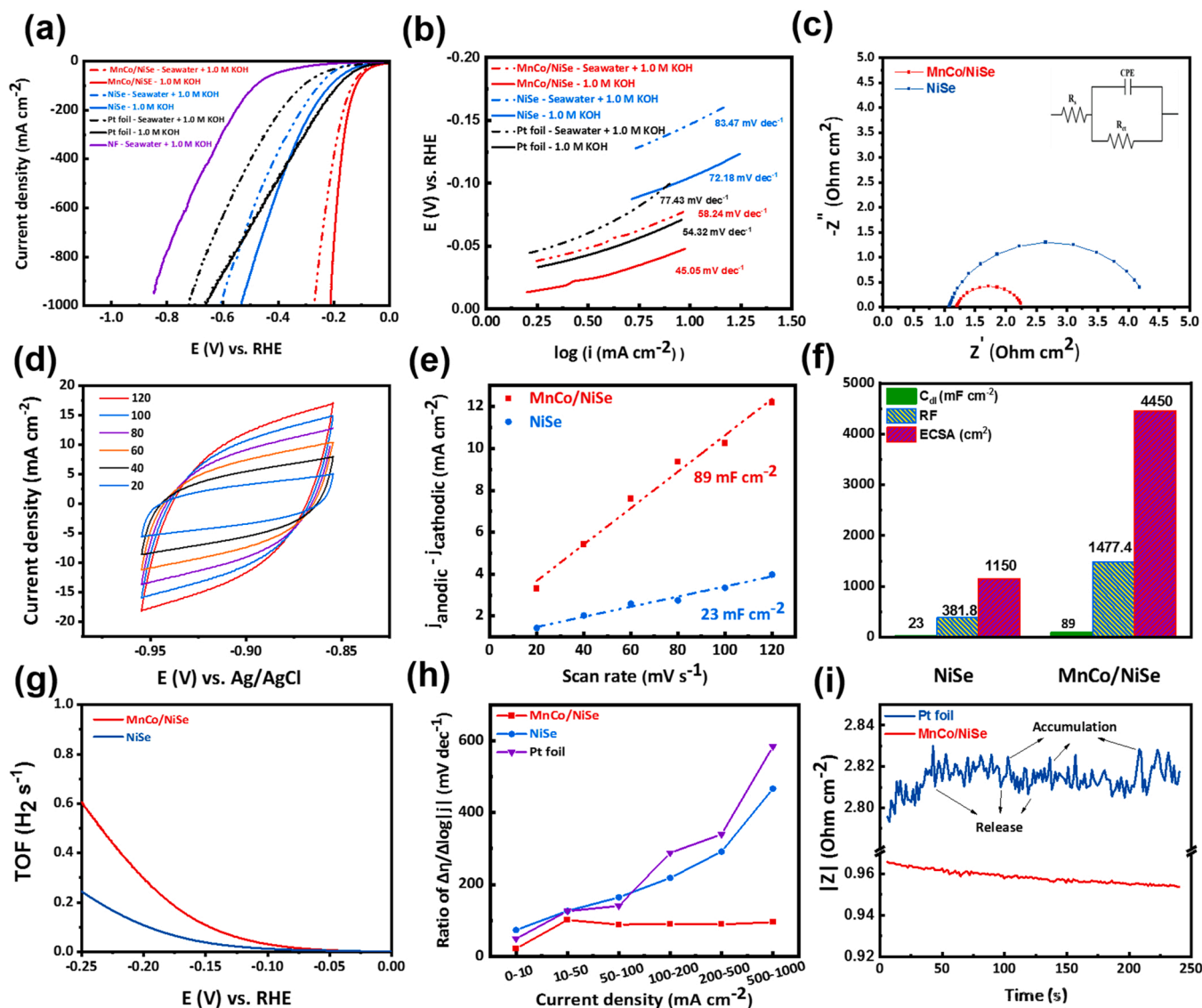
Fig. 4. Electrocatalytic activity for the HER. (a) HER LSV curves for Ni foam, MnCo/NiSe, Pt foil, and NiSe electrodes in 1.0 M KOH and 1.0 M KOH + seawater electrolyte with a scan rate of 5 mV s^{-1};(b) Tafel slopes for the electrocatalysts extracted from (a); (c) Nyquist curves of MnCo/NiSe and NiSe electrodes at an overpotential of − 200 mV; (d) CV curves of MnCo/NiSe in different scan rates; (e) Plots presentation the extracted C$_{dl}$ values for the MnCo/NiSe and NiSe electrocatalysts' (f) C$_{dl}$ and ECSA of the MnCo/NiSe and NiSe electrodes; (e) Ratios of Δη/Δlog|j|in various ranges of current density in 1.0 M KOH for MnCo/NiSe, NiSe, and Pt foil; (g) TOF curves for MnCo/NiSe and NiSe electrocatalysts; (h) Ratios of Δη/Δlog|j|in various ranges of current density for MnCo/NiSe, NiSe, and Pt foil; (i) Operando dynamic specific resistance at an HER overpotential of − 400 mV in 1.0 M KOH.

Furthermore, to investigate the HER reaction mechanism and estimate the kinetics in alkaline water (seawater), Tafel slopes obtained from LSV curves (Fig. 4a) are presented in Fig. 4b. As it is evident, Tafel slope values of MnCo/NiSe in both electrolytes of alkaline water (45.0 mV dec^{-1}) and alkaline seawater (58.2 mV dec^{-1}) are lower than their corresponding NiSe values (72.1 and 83.4 mV dec^{-1} for both solutions, respectively). Interestingly, the MnCo/NiSe electrode also showed superior Tafel slopes to Pt foil in both conditions (53.3 in 1.0 M KOH and 77.4 mV dec^{-1} in 1.0 M KOH + Seawater). Moreover, MnCo/NiSe reveals much better HER kinetic than other tested as-fabricated electrodes, which can be due to the synergistic effect between the two layers of MnCo and NiSe, which optimizes the electronic structure and improves the electrical conductivity. In addition, the excellent kinetics of the MnCo/NiSe electrode can confirm the beneficial effect of its microsphere containing interconnected nanosheets morphology, which could significantly improve the kinetics of reactions by easy adsorption of the electrolyte and rapid release of gas bubbles. Noticeably, the values of Tafel slopes for MnCo/NiSe reveal that the HER rate-determining step

on the MnCo/NiSe is the desorption of atomic hydrogen from the surface (Volmer–Heyrovsky mechanism) [37]. For the more profound investigation of the HER kinetic for the as-mentioned electrocatalysts, electrochemical impedance spectroscopy (EIS) was employed. The R$_{ct}$ values were obtained from the diameter of semicircles in the EIS Nyquist fitting plot in 1.0 M KOH + seawater for both MnCo/NiSe and NiSe (Fig. 4c); The R$_{ct}$ values for MnCo/NiSe and NiSe are 1.24 and 3.1 Ω cm^2, which it is entirely in accordance with the obtained results from the Tafel slope results.

To examine the improvement of the intrinsic properties of NiSe induced by the addition of MnCo, the ECSA values of as-fabricated electrodes were assessed. The ECSA and roughness factor (RF) are vital factors that significantly can impact electrocatalytic efficiency [38]. To attain the ECSA and RF, at first, the double-layer capacitance (C$_{dl}$) must be calculated. Fig. 4e and f illustrate C$_{dl}$, ECSA, and RF values of MnCo/NiSe and NiSe, obtained from their CV curves (Fig. 4d and S8, the calculation methods for C$_{dl}$, ECSA, and RF are presented in the Experimental Section above). According to Fig. 4e and f, MnCo/NiSe has

almost 4 times higher C_{dl} and ECSA values (89 mF cm^{-2} and 4450 cm^2, respectively) than NiSe (23 mF cm^{-2}, 1150 cm^2), which indicates the significantly improved morphology and increased active catalytic sites after adding the MnCo layer on NiSe, consequently, more efficient catalytic performance can be achieved. It should be noted that the RF value for MnCo/NiSe (1477.4) is also much higher than that of NiSe (281.8), which reveals that MnCo/NiSe has a much rougher surface, consequently more favorable for adsorption and diffusion of active species in the electrolyte.

In addition, the two methods that have been highly proposed that can accurately indicate the inherent activity of an electrocatalyst are the TOF and normalizing the current with the actual ECSA. Both parameters are derived directly from the ECSA value [39]. It is found that just reporting the amount of overpotential at a constant current density obtained from the LSV curves cannot accurately display the intrinsic activity of the electrocatalyst because of its dependence on catalyst loading. The ECSA-normalized specific activity and the associated overpotential at any set current density will not change regardless of the loading of the electrocatalyst, which can be a good indicator for showing the intrinsic mass transfer capability of an electrocatalyst [40]. Another intrinsic catalytic activity indicator is TOF, a quantity originating from the current density at a given potential and the surface concentration or the number of metal sites. The TOF, as the specific activity, cannot be affected by electrocatalyst loading and can demonstrate intrinsic activity [39]. Fig. S9 exhibits the ECSA-normalized LSVs of MnCo/NiSe and NiSe electrodes. As can be seen, MnCo/NiSe still exhibits superior HER performance than NiSe after ECSA normalization. Fig. 4g also shows the TOF plot for MnCo/NiSe and NiSe. The TOF plot also confirmed the higher activity of MnCo/NiSe than NiSe at different applied overpotentials for HER. The TOF of MnCo/NiSe (0.6 s^{-1}) was significantly higher than that of NiSe (0.241 s^{-1}) at the HER overpotential of - 0.250 mV. The results indicate that the MnCo/CuNiP electrocatalyst displayed superior HER electrochemical properties (The calculation method for TOF and ECSA-normalized specific activity are presented in Experimental section above). The TOF and ECSA-normalized specific activity both reveals the significant effect of adding MnCo to NiSe, which remarkably improved the HER intrinsic activity of NiSe by increasing its active catalytic sites on the surface of MnCo/NiSe electrocatalyst, consequently enhancing the electrocatalytic performance.

Mass transfer is another crucial factor in determining an electrocatalyst's HER performance, especially at high current densities. The proportion of overpotential to current density ($\Delta\eta/\Delta\log|j|$) was employed to evaluate the mass transfer of the MnCo/NiSe, NiSe, and Pt foil electrocatalysts and assess how much overpotential is required when current density grows, which could be an indicator to estimate the performance of a catalyst at high current densities and see if it is suitable for practical use or not [41]. It should be noted that for an electrocatalyst to meet the prerequisites required for practical applications, the ratio of $\Delta\eta/\Delta\log|j|$ at high current densities must be low. As displayed in Fig. 4h, for MnCo/NiSe in alkaline water (Fig. S10 is in alkaline seawater), by increasing current density, a small ratio at various current density ranges is obtained (22.0–89.5 mV dec^{-1} for ranges of 0–10 and 200–500 mA cm^{-2}, respectively), which much less than those for NiSe in the same range (139.1–364.18 mV dec^{-1}) and Pt foil (94.2–462.5 mV dec^{-1}) in both electrolytes. As can be seen in alkaline water and seawater, when the current density is very large (i.e., more than 200 mA cm^{-2}), HER performance of NiSe and especially Pt foil are strongly affected and possesses a much higher $\Delta\eta/\Delta\log|j|$ ratios than MnCo/NiSe. From the above electrochemical results, it is clear that adding MnCo to the NiSe has a critical impact on the interaction between the electrocatalyst and intermediates at the interface and, therefore, on the large-current-density HER performance of the electrocatalyst.

Superaerophobicity and superhydrophilicty are among the essential features that should be evaluated along with other factors to estimate the catalytic performance of an electrode. It has been found that

catalysts with a smooth surface or a weak ability to detach gas bubbles offer low catalytic performance. In smooth surface catalysts, when electrochemical reactions are performed on the electrode surface, due to the weakness in the rapid release of gas bubbles, these bubbles accumulate on the surface and then combine to form an unwanted gas layer that prevents contact of the surface and electrolyte, therefore, charge transfer resistance through electrode increases and mass transfer decreases; consequently, the electrocatalytic performance is severely affected, and the overpotential is impressively increased [42]. To examine the gas bubble detachment behavior and superaerophobicity of the MnCo/NiSe and Pt foil electrocatalysts at extreme conditions, a large overpotential of − 400 mV was applied to examine dynamic specific resistance. As demonstrated in Fig. 4i, |Z| value for Pt foil experienced wild fluctuations; in the meantime, the specific resistance values for the MnCo/NiSe electrode remained rather constant during 240 s. The upward peaks are associated with the formation of bubbles and their combination on the electrocatalyst surface. The sudden decline in the |Z| values relates to the detachment of as-generated bubbles [43,44].

Overall, the high HER activity of MnCo/NiSe could be ascribed to three main reasons: (1) A significant increase of ECSA value after the addition of MnCo to NiSe, which can provide much higher HER active sites; (2) After the addition of MnCo to NiSe, according to the R_{ct} values extracted from Nyquist plot for MnCo/NiSe considerably decreased, which show higher electrical conductivity of MnCo/NiSe rather than NiSe. The reason behind the higher conductivity of NiSe could be related to the nature of heterostructured nanomaterials, which due to the presence of multiple interfaces, have more electronic paths provided for catalytic reactions; (3) The Superaerphobicity/superhydrophilicity feature of MnCo/NiSe was also proved by Operando dynamic specific resistance test. This feature, in which morphology plays a key role in it, significantly can improve the catalytic activity of an electrocatalyst and cause better reaction kinetics by a fast detachment rate of gaseous bubbles from the surface of the electrode.

3.2.2. OER performance of MnCo/NiSe in alkaline seawater and freshwater

The OER performance of the MnCo/NiSe and NiSe electrocatalysts was estimated by LSV curves (Figs. 5a and S11) in alkaline water (seawater). Obviously, MnCo/NiSe displays superior OER activity in various ranges of current density than NiSe in both electrolytes. MnCo/NiSe electrocatalyst needs only overpotentials of 225.8, 340.4, and 370.7 mV in alkaline water and 261.3, 419.4, and 460.2 mV in alkaline seawater for attaining the current densities of 10, 500, and 1000 mA cm^{-2}, respectively, less than the maximal potential (~490 mV) for preventing the generation of hypochlorite. At the same current densities order, NiSe possesses overpotentials of 341.4, 570.3, and 780.2 mV in alkaline water and 384.3, 661.7, and 930.4 mV in alkaline seawater. Clearly, the OER LSVs for MnCo/NiSe electrode have a peak (located in 1.37 V vs. RHE in 1.0 M KOH) in both solutions, which is located in a higher current density and less potential than NiSe (1.44 V vs. RHE). The peak related to NiSe could be ascribed to the oxidation peak of Ni^{2+}/Ni^{3+} for OER [45]. Prior studies on Ni-based anodic electrodes have identified higher oxidation states of transition metals (e.g., Ni^{+3}) and NiOOH species as essential active sites for electro-oxidation reactions (e.g., OER) [46]. According to XPS results, In MnCo/NiSe, the peaks related to Ni^{+2}/Ni^{+3}, Co^{+2}/Co^{+3}, and Mn^{+2}/Mn^{+3} are detectable, which can function as active sites for OER by forming NiOOH, MnOOH, and CoOOH. On the other hand, it has been found that Co can increase the phase transformation of Ni(OH)$_2$ to NiOOH and lower the redox potential of Ni^{3+}/Ni^{2+} and ultimately improve OER [47,48]. Additionally, up to now, Co and Mn-based electrodes are regarded as highly active OER catalysts. An agitated distribution of cations in metals with a mixed-valence state, for example, Co^{+2} and Co^{+3} for Co and Mn^{+2}, Mn^{+3}, and Mn^{+4} for Mn, can result in adjustable electronic configurations of the materials and facilitate easy movement of electrons and cause high electrocatalytic conductivity [49].
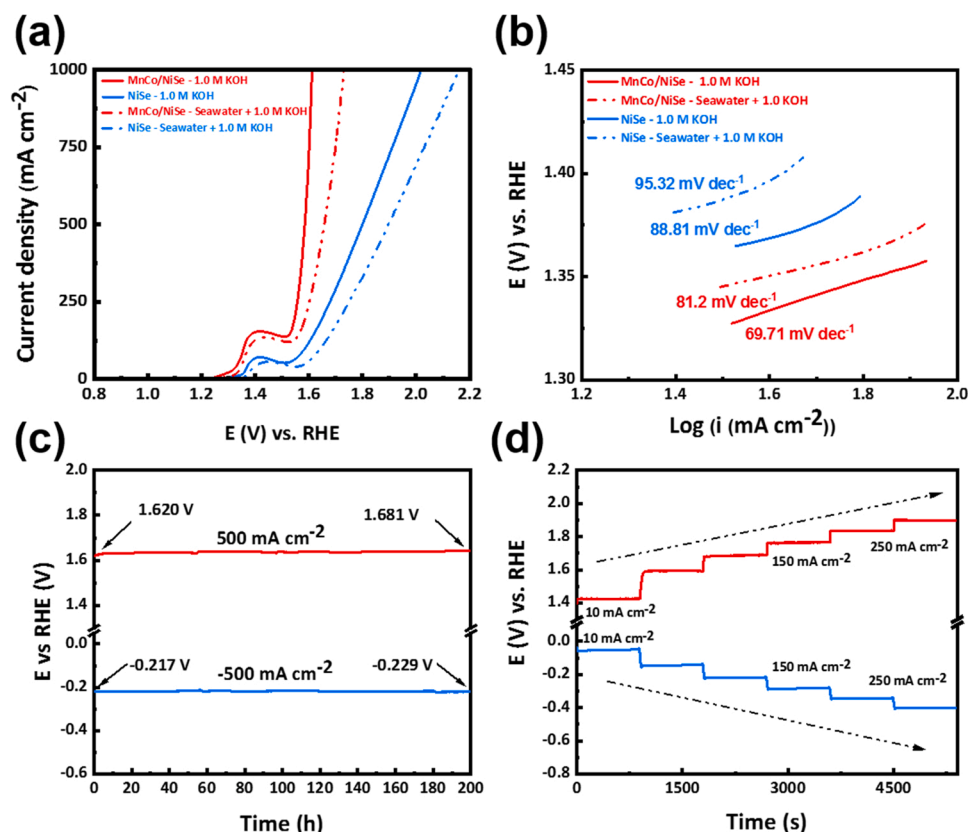
Fig. 5. Electrocatalytic activity for the OER; (a) Polarization curves for the OER on the MnCo/NiSe and NiSe electrocatalysts in 1.0 M KOH and 1.0 M KOH + seawater electrolytes with a scan rate of 5.0 mV s^{-1}; (b) Tafel plots for the electrocatalysts derived from (a); Chronopotentiometry stability test results for HER and OER in 1.0 M KOH + seawater solution (c), (d) Multi-Step chronopotentiometry tests results (without iR correction) under cathodic and anodic currents for MnCo/NiSe results in 1.0 M KOH + Seawater.

Fig. 5b also shows Tafel curves obtained from corresponding OER LSVs to investigate further OER kinetics on the surface of the MnCo/NiSe and NiSe electrocatalysts in alkaline water and seawater. The MnCo/NiSe electrocatalyst has smaller OER Tafel slopes in alkaline water (69.7 mV dec^{-1}) and alkaline seawater (81.2 mV dec^{-1}) and functions faster in terms of reaction kinetics compared to NiSe (88.8 and 95.3 69.7 mV dec^{-1} in both solutions, respectively). According to the results, the addition of MnCo to the NiSe can significantly improve the properties of OER. It should be noted that the MnCo/NiSe electrocatalyst performed better than not only NiSe but also other previously reported OER electrocatalysts (Table S1).

3.2.3. Post-OER and HER and stability performance of MnCo/NiSe in alkaline seawater

For an efficient water electrolysis system, the stability of the electrode also plays an important role. As shown in Fig. 5c, during the chronopotentiometry (CP) test, the MnCo/NiSe electrode sustained a 500 mA cm^{-2} anodic and cathodic current density for 200 h in alkaline seawater, which indicates its highly stable performance and corrosion resistance properties in anodic and cathodic conditions. Several reasons exist for the highly stable performance of the as-produced MnCo/NiSe electrocatalyst. Firstly, due to the formation of microsphere/nanosheet morphology, MnCo/NiSe electrocatalyst showed a high ability to reduce the adhesion of bubbles on the surface and easier adsorption of active species in the electrolyte. Rapid bubble separation can be effective in improving catalytic stability. Secondly, the dissolved cations in the alkaline electrolyte react with the OH$^-$ agent, re-deposit on the electrode surface, and serve as a protective layer against degradation [50].

Mass transportability is also vital for an electrocatalyst. Up to now, the multistep chronopotentiometry technique has been employed to approve both mass transportability and catalytic stability. As demonstrated in Fig. 5d, it can be seen that by shifting the current density from − 10 to − 250 mA cm^{-2} for HER and 10–250 mA cm^{-2} for OER every 15 min, the high mass transport capability is exhibited by the instant

response in potential and that the potential for each step stays steadily. Finally, the CV stability test was also used to estimate the HER durability of the MnCo/NiSe electrocatalyst under potential changes, as exhibited in Fig. S17. As can be seen, after 5000 cycles (5000 cycles between the ranges of 0 to −0.2 V vs. RHE with a scan rate of 100 mV s^{-1}), the HER LSV curve of MnCo/NiSe electrocatalyst shows excellent durability with negligible degradation. Noticeably, the catalytic performance of the MnCo/NiSe electrocatalyst has enhanced after 3000 cycles, which could be due to better infiltration of alkaline solution and better interaction at the interface between the active species and electrocatalyst electrode.

Based on the FESEM and TEM images for post-OER and post-HER stability (Fig. S12), almost no morphological changes were observed, proving the excellent morphological stability of the MnCo/NiSe catalyst. The FESEM-EDS (Figs. S13 and S14) analysis also indicates that the even dispersion of Mn, Co, Ni, and Se in the MnCo/NiSe surface remains unchanged. Figs. S15 and S16 also show post-OER and post-HER XPS spectrums. Results indicate that all the original valences of Ni, Mn, Se, and Co are kept. However, as presented in Fig. S15a for the post-OER Ni 2p spectrum, the ratio of Ni^{3+}/Ni^{2+} is dramatically increased, revealing that most Ni^{2+} converted to Ni^{3+}, as previously discussed, could act as active catalytic sites and improve catalytic OER activity. Previous studies have proved that the increased Ni^{3+} species will raise eg orbitals occupancy of surface nickel cations and exist more electronic configuration of Ni^{3+} (t_{2g}^6), which displays higher OER activity and efficiently regulate the electronic arrangement of electrocatalyst and boosts the adsorbing capacity of OER intermediate species [51]. A comparison of the Co 2p spectrum before and after the OER stability test (Fig. S15c) reveals an obvious increase in the amount of Co^{3+}, which indicates the considerable post-OER oxidation of Co^{2+} to Co^{3+}. For post-OER in Mn 2p spectrum, the Mn^{2+} ions are highly oxidized to high-valent Mn ions (Mn^{3+} and Mn^{4+}) after the OER stability test (Fig. S15d). According to the post-OER investigation in Fig. S15, Ni^{3+}, Mn^{3+}, and Co^{3+} are the main Ni, Mn, and Co ions after OER stability. In addition, the co-presence of Mn^{3+} and Co^{3+} active sites aid in diminishing the

Jahn-Teller distortion in the MnCo/NiSe electrocatalyst and attracts OER species to the electrocatalyst surface [52]. The presence of Mn³⁺/Mn⁴⁺ and Co²⁺/Co³⁺ redox couples may offer donor-acceptor chemisorption spots for the reversible adsorption/desorption of oxygen [53]. Additionally, the polaron hopping conduction mechanism may allow for the movement of electrons with highly reduced activation energy across Mn cations with various valence states (Mn³⁺ and Mn⁴⁺), enhancing the electrical conductivity of the MnCo/NiSe electrocatalyst [54]. Overall, no apparent changes were observed in the post-OER Se 3d and post-HER XPS spectrum of the MnCo/NiSe electrocatalyst, indicating its high stability and durability in 1.0 M KOH + seawater.

X-ray absorption spectroscopy (XAS) is a powerful method to analyze the local structure of materials. The X-ray absorption near edge structure (XANES) region of XAS can supply information on the oxidation state of the absorbing atom. To further probe the structural variation of different samples, XANES spectrums of Ni, Mn, and Co in MnCo/NiSe K-edge before and after the OER stability test were measured. In Fig. 6a higher energy shift of Ni L-edge XAS after OER reflects an increased Ni valence on the surface [55]. In Fig. 6b and c, it is also obvious that Mn and Co L-edge XAS experienced higher energy shift after the OER stability test, which shows an increased Mn and Co valences on the surface of MnCo/NiSe electrocatalyst. Overall, The Mn, Co, and Ni rising edge shifts to higher photon energy values after OER, indicating a higher oxidation state (Ni⁺³/ NiOOH, Mn⁺³/ MnOOH, and Co⁺³/ CoOOH) and in accordance with XPS spectra where Mn 2p, Co 2p, and Ni 2p peaks shift to higher binding energies. As previously discussed, NiOOH, MnOOH, and CoOOH are considered active spots for OER and can promote kinetic reactions by providing abundant active sites [56,57]. To further trace the local environment and bonding structure variations during OER catalysis, we in-depth analyzed the extended X-ray absorption fine structure (EXAFS) spectra of MnCo/NiSe before and after the OER stability test by using Fourier transform (FT). In the FT curves of the k³-weighted Ni K-edge EXAFS (Fig. 6d), the peak located at about 1.1 Å and 2.0 Å belongs to the Ni-Se and Ni-Ni bonds while a new peak at around 1.6 Å appears after the electrochemical oxidation, corresponding to the Ni-O/OH bonds of the in-situ-generated surface

oxide/hydroxide after OER stability test. The FT of EXAFS spectra collected on MnCo/NiSe showed typical features of layered hydroxides (Fig. 6e and f) in both edges, Co−K and Mn−K. Two prominent peaks were identified: a M−O peak of around 1.87 Å (1.2 Å for Co), and a M−M peak of around 2.42 Å (2.05 Å for Co), where M is either Mn or Co [58]. Moreover, Mn, Co, and Ni exhibit decreasing bond lengths from metal foils, samples before OER to samples after OER, indicating higher oxidation states, in accordance with XPS spectra where Mn 2p, Co 2p, and Ni 2p peaks shift to higher binding energies [59]. Therefore, the XPS and XAS results systematically validate the electronic modulation and chemical coupling effects in MnCo/NiSe, which significantly modifies the local configurations of both MnCo and NiSe structures. These modulated electronic properties of MnCo/NiSe should alter the adsorption/desorption properties of reactants and therefore might contribute to enhancing electrocatalytic performance.

3.2.4. Cell performance of MnCo/NiSe in alkaline seawater

Using the MnCo/NiSe electrocatalyst, a cell was built to evaluate further the water (seawater) electrolysis performance of the MnCo/NiSe electrocatalyst as the anode and cathode (MnCo/NiSe || MnCo/NiSe). Fig. 7a demonstrates the LSV curves of the MnCo/NiSe || MnCo/NiSe in alkaline water and seawater solutions. Superbly, the bifunctional MnCo/NiSe electrocatalyst displayed outstanding electrochemical performance with operating voltages of 1.41, 1.67, 1.88, and 1.92 V in 1.0 M KOH and 1.44, 1.86, 1.99, and 2.11 V to respectively touch current densities of 10, 100, 500, and 1000 mA cm⁻² (video S1) which is much less than those of previously reported bifunctional electrocatalysts in alkaline water and seawater (Table S1). Therefore, the MnCo/NiSe || MnCo/NiSe configuration demonstrated high electrochemical performance in both alkaline water and alkaline seawater. Moreover, the long-standing stability of the MnCo/NiSe || MnCo/NiSe cell system was estimated by the CP test, as displayed in Fig. 7b. Throughout continuous running for 200 h at 500 mA cm⁻² in 1.0 M KOH + seawater, the system's voltage slightly increased (under 8%). Overall, MnCo/NiSe//MnCo/NiSe electrolyzer showed highly stable long-term performance. Experimental measurements and theoretical calculations of evolved hydrogen gas
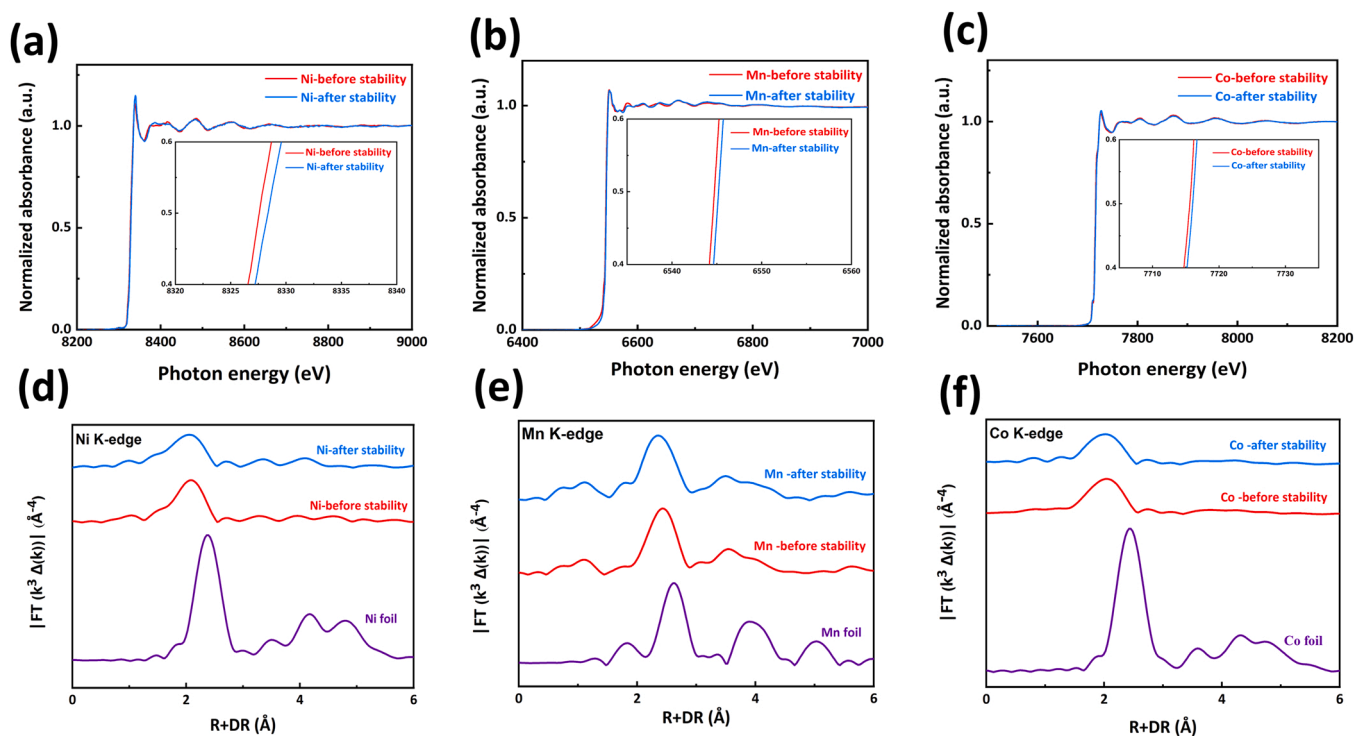

Fig. 6. Normalized Ni (a), Mn (b), and Co (c) K-edge XANES spectra of MnCo/NiSe before after the OER stability test. Ni (d) Mn (e), and Co (f) K-edge FT-EXAFS spectra of MnCo/NiSe before and after the OER stability test.
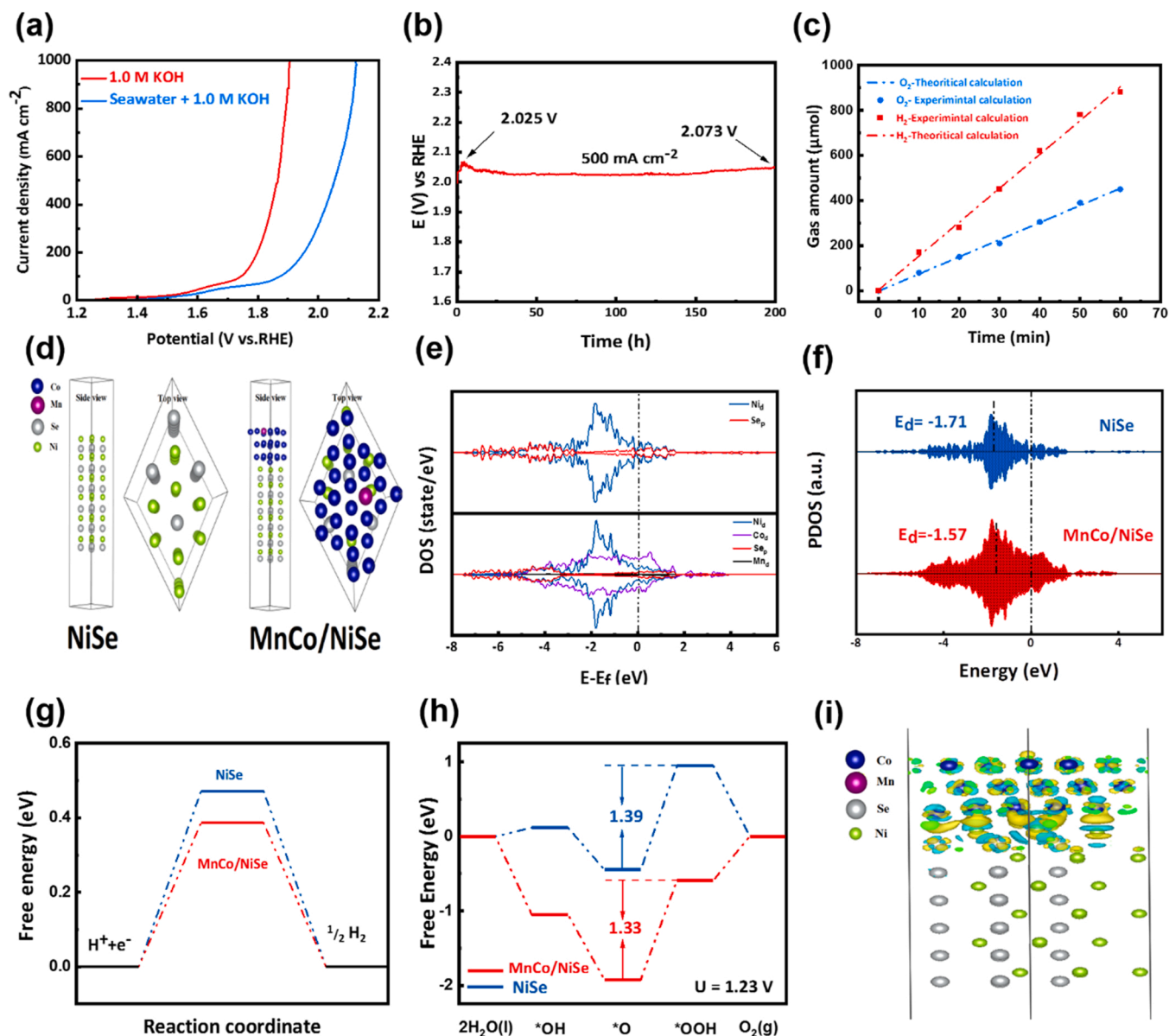
Fig. 7. (a) Overall water splitting LSV curves of the MnCo/NiSe ‖ MnCo/NiSe electrolyzer system in 1.0 M KOH and 1.0 M KOH + seawater; (b) Chronopotentiometry stability test of MnCo/NiSe ‖ MnCo/NiSe Cell at a constant current density of 500 mA cm^{-2} in 1.0 M KOH + Seawater electrolyte (without iR correction); (c) Current efficiency of MnCo/NiSe electrocatalyst at a current density of 50 mA cm^{-2}; (d) The optimized geometry of NiSe and MnCo/NiSe models, (e) Densities of states (DOSs) and (f) Partial densities of states (PDOSs) for d orbitals of NiSe and MnCo/NiSe, (g) Free-energy diagrams for H adsorption in HER, (h) Free-energy pathway for O, OH and OOH adsorptions in OER on the surfaces of NiSe and MnCo/NiSe, and (i) Electron density redistribution of the interface made by MnCo and NiSe. Green and yellow colors display regions of lowering and enhancement of electron density, respectively.

were performed to assess the Faradaic efficiency at a current density of 50 mA cm^{-2} by gas chromatography. The comparison between the experimental outcomes and the theoretical value indicates that the Faradaic efficiency is 97.6% for MnCo/NiSe electrocatalyst in alkaline seawater (Fig. 7c).

Supplementary material related to this article can be found online at doi:10.1016/j.apcatb.2022.122355.

3.2.5. First principle calculations

Here, we applied DFT calculations to get a deeper insight into the electronic role made by MnCo on the catalytic activity of the given system. To do this, at first, our initial model was evaluated by going from the bulk to the surface structures considering the different thicknesses of NiSe with the most abundant planes, that are, (101), (102), (110), and (002). According to our calculations, the surface energies [24] of these

systems having five to two layers range 0.25–0.82 J/m^2 (corresponds to 0.01–0.05 eV/A^2). Here, one of the more stable planes (002) having three layers and the minimum lattice mismatch with MnCo was considered to make MnCo/NiSe heterostructure Fig. 7d. Then, the partial density of states (PDOS) of the given systems in both models (NiSe and MnCo/NiSe) were calculated to explore the electronic effects made by the MnCo layers. As displayed in Fig. 7e, the MnCo/NiSe heterostructure generates a higher density of carriers around the Fermi level. Specifically, D-states in this system mainly supported by Co atoms shift closer to the Fermi level rather than those of NiSe, indicating the significantly improved conductivity of the given heterostructure. Moreover, as seen in this figure, the DOS of D-states assigned to the Ni atoms are further amplified, showing the synergetic role revealed by MnCo. Obviously, these are favorable for the catalytic processes in which charge transfer plays an important role [60]. In addition, our

analysis of the projected d-band partial density of states (PDOS), reported in Fig. 7f, shows that the d-band center of the NiSe was significantly toward the Fermi level (upshifted) by incorporating the MnCo into the initial structure. This is in good agreement with our XPS results, that is, binding energy peak of the base metal (Ni) shifts positively. Indeed, the incorporation of Co decreases electron density around the Ni atoms from which the binding energy increases. This issue is discussed in detail by plotting the electron density differences at the interface of the MnCo/NiSe heterostructure.

Thus, this upshifting amplifies the bonding strength between species and further increases the stability of the adsorption states. Indeed, the mechanism relevant to this phenomenon suggests that antibonding states can be pushed above the Fermi energy when the d-band states are close to the Fermi energy, leading to decreases in the Pauli repulsion and, consequently, increases the bond strength between the adsorbate and the surface of catalyst [61].

Evaluation of Gibbs free-energy change of the HER, i.e. hydrogen adsorption (ΔG_{H*}), and those steps related to the OER process are one of the most fundamental approaches to studying the performance of catalysts. It is well accepted that ΔG_{H*} should be close to zero for an efficient HER process [62]. As shown in Fig. 7g, the ΔG_{H*} of the MnCo/NiSe heterostructure is closer to zero (by about 0.1 eV) than that of NiSe, agreeing with the literature reported for the HER process over the NiSe$_2$ compound [63]. This clearly shows that the bond strength between the adsorbate H* and the surface of the catalyst is strengthened, thus, a high efficient HER performance is expected [62]. On the other hand, our results highlight the important role of MnCo in the efficiency of OER catalysis. Interestingly, it is observed (Fig. 7h) that the thermodynamics are processed over MnCo/NiSe much better than those of the NiSe. In addition, the barrier energy of the rate-determining step, which is the third proton-electron transfer step, transitions from O* to OOH* [64], decreases by about 0.06 eV over the MnCo/NiSe. This discloses a more favorable kinetics for the OER process of the MnCo/NiSe heterostructure than that of the NiSe. These results rationalize the improved OER process and are in accordance with the OER activity of the Ni-based catalysts [65].

We have future plotted the charge density differences of the systems to better understand the process of charge transfer between species (Fig. 7i). Clearly, the representation of the MnCo/NiSe system shows that there are charge donations mainly from the Ni atoms, which are closer to the interface, to the Co atoms, confirming shifting the binding energy peaks observed in XPS results as mentioned above. In addition, using our calculations we found substantial charge transfer on the adsorption of H, OH, O, and OOH species at both Ni and Co binding sites (Fig S18). For these cases, the charge accumulation around the species is generally amplified by introducing the MnCo into the NiSe, increasing the reactivity of the MnCo/NiSe rather than the NiSe system. Therefore, the DFT results show that the MnCo facilitates charge transfer and optimizes the d-band center, leading to increased catalytic performance of both the HER and OER processes.

A facile two-step electrodeposition procedure for fabricating a novel heterostructured MnCo/NiSe electrocatalyst on Ni Foam was employed for efficient alkaline seawater splitting. The superb performance MnCo/NiSe could be attributed to: (1) heterostructured MnCo/NiSe by having superaerophobicity/superhydrophilicity properties caused by its unique 3-D morphology of microspheres containing interconnected nanosheets, could in addition to improving catalytic stability because of the easy detachment of gas bubbles and exposing more catalytically active sites to active species within the electrolyte also greatly improved mass transfer properties at high current densities; (2) the addition of MnCo to NiSe caused a synergistic effect between the two structures and by increasing the electronic path, it could tune the electronic arrangement and significantly increase the kinetics of electrochemical reactions on the electrode surface; (3) The hydroxide layer (NiOOH, MnOOH, CoOOH) generated on the surface of MnCo/NiSe during full water electrolysis boosted the movement of electrones, consequently

enhancing the electrocatalytic performance of MnCo/NiSe [66]; (4) The as-fabricated MnCo/NiSe electrocatalyst demonstrated highly stable performance and resistance to degradation in alkaline seawater, making it a suitable electrocatalyst for seawater splitting; (5) DFT calculations exposed the fact that there is a synergistic effect between MnCo and NiSe, which improves the electronic construction with a upshift of the d band center and optimizes the reactivity during HER and OER processes.

4. Conclusion

In summary, heterostructured MnCo/NiSe electrocatalyst with microspheres containing interconnected nanosheets morphology was successfully synthesized on a Ni foam substrate via the electrodeposition technique, which displays excellent bifunctional electrolytic activity for both HER and OER in alkaline water (seawater) electrolyte. Benefiting from the superaerophobicity/superhydrophilicity features, superior electrical conductivity, and high inherent activity, the constructed MnCo/NiSe electrocatalyst possesses an exceptional HER (182.8 and 211.6 mV in alkaline water and 216.3 and 270.1 mV in alkaline seawater to run current densities of -500 and -1000 mA cm^{-2} respectively) and OER (340.4 and 370.7 in 1.0 M KOH and 419.4 and 460.2 mV in 1.0 M KOH + seawater to attain current densities of 500 and 1000 mA cm^{-2}, respectively) performance. MnCo/NiSe || MnCo/NiSe cell system also possessed low cell voltages of 1.41, 1.67, 1.88, and 1.92 V in 1.0 M KOH and 1.44, 1.86, 1.99, and 2.11 V to respectively touch current densities of 10, 100, 500, and 1000 mA cm^{-2}. Results indicated that adding MnCo to the NiSe could significantly increase the value of accessible catalytic active sites for HER and OER, tuning the electronic structure to improve electrical conductivity and optimize the morphology for better wettability behavior. DFT calculations, in line with XPS results, showed a better electrochemical performance due to enhanced electron transfer from NiSe to the MnCo, facilitating the HER and OER processes. Besides, The MnCo/NiSe electrode also showed robust stability in 1.0 M KOH + seawater, indicating its excellent corrosion resistance. To sum up, owing to the facile synthesis procedure, outstanding electrocatalytic activity, and stability of MnCo/NiSe, this study may provide a basis for designing electrocatalysts for industrial water (seawater) splitting on a large scale.

CRediT authorship contribution statement

Reza Andaveh: Formal analysis, Investigation, Methodology, Writing – original draft, Conceptualization, Resources. **Alireza Sabour Rouhaghdam:** Funding acquisition, Supervision, Project administration. **Jianping Ai:** Investigation, Software, Conceptualization, Methodology. **Meysam Maleki:** Investigation, Software, Conceptualization, Methodology, Writing – original draft. **Kun Wang:** Investigation, Conceptualization, Methodology. **Abdolvahab Seif:** Software, Investigation, Validation, Writing – review & editing. **Ghasem Barati Darband:** Conceptualization, Validation, Data curation, Supervision, Project administration, Writing – review & editing. **Jinyang Li:** Data curation, Validation, Formal analysis, Funding acquisition, Writing – review & editing.

Declaration of Competing Interest

The authors declare that they have no known competing financial interests or personal relationships that could have appeared to influence the work reported in this paper.

Data availability

Data will be made available on request.

Acknowledgments

Appendix A. Supplementary material

Supplementary data associated with this article can be found in the online version at doi:10.1016/j.apcatb.2022.122355.

References

[1] B. Sørensen, Guest editorial: renewables and hydrogen energy technologies for sustainable development, Int. J. Energy Res. 32 (2008) 367–368, https://doi.org/10.1002/er.1370.

[2] C.-J. Winter, Hydrogen energy — abundant, efficient, clean: a debate over the energy-system-of-change, Int. J. Hydrog. Energy 34 (2009) S1–S52, https://doi.org/10.1016/j.ijhydene.2009.05.063.

[3] S. Sultan, J.N. Tiwari, A.N. Singh, S. Zhumagali, M. Ha, C.W. Myung, P. Thangavel, K.S. Kim, Single atoms and clusters based nanomaterials for hydrogen evolution, oxygen evolution reactions, and full water splitting, Adv. Energy Mater. 9 (2019), 1900624, https://doi.org/10.1002/AENM.201900624.

[4] E. Asghari, M.I. Abdullah, F. Foroughi, J.J. Lamb, B.G. Pollet, Advances, opportunities, and challenges of hydrogen and oxygen production from seawater electrolysis: an electrocatalysis perspective, Curr. Opin. Electrochem. 31 (2022), 100879, https://doi.org/10.1016/j.coelec.2021.100879.

[5] Z. Huang, S. Yuan, T. Zhang, B. Cai, B. Xu, X. Lu, L. Fan, F. Dai, D. Sun, Selective selenization of mixed-linker Ni-MOFs: NiSe2@NC core-shell nano-octahedrons with tunable interfacial electronic structure for hydrogen evolution reaction, Appl. Catal. B Environ. 272 (2020), 118976, https://doi.org/10.1016/J.APCATB.2020.118976.

[6] L. Wu, L. Yu, B. McElhenny, X. Xing, D. Luo, F. Zhang, J. Bao, S. Chen, Z. Ren, Rational design of core-shell-structured CoPx/FeOOH for efficient seawater electrolysis, Appl. Catal. B Environ. 294 (2021) 120256, https://doi.org/10.1016/J.APCATB.2021.120256.

[7] D. Guo, D. Zeng, Z. Wan, Y. Li, B. Xi, C. Wang, A CoN-based O.E.R. electrocatalyst capable in neutral medium: atomic layer deposition as rational strategy for fabrication, Adv. Funct. Mater. 31 (2021), 2101324, https://doi.org/10.1002/adfm.202101324.

[8] L. Bigiani, D. Barreca, A. Gasparotto, T. Andreu, J. Verbeeck, C. Sada, E. Modin, O.I. Lebedev, J.R. Morante, C. Maccato, Selective anodes for seawater splitting via functionalization of manganese oxides by a plasma-assisted process, Appl. Catal. B Environ. 284 (2021), 119684, https://doi.org/10.1016/J.APCATB.2020.119684.

[9] J. Liu, X. Liu, H. Shi, J. Luo, L. Wang, J. Liang, S. Li, L.M. Yang, T. Wang, Y. Huang, Q. Li, Breaking the scaling relations of oxygen evolution reaction on amorphous NiFeP nanostructures with enhanced activity for overall seawater splitting, Appl. Catal. B Environ. 302 (2022), 120862, https://doi.org/10.1016/J.APCATB.2021.120862.

[10] C. Wang, H. Shang, L. Jin, H. Xu, Y. Du, Advances in hydrogen production from electrocatalytic seawater splitting, Nanoscale 13 (2021) 7897–7912, https://doi.org/10.1039/d1nr00784j.

[11] Y. Li, Y. Sun, Y. Qin, W. Zhang, L. Wang, M. Luo, H. Yang, S. Guo, Recent advances on water-splitting electrocatalysis mediated by noble-metal-based nanostructured materials, Adv. Energy Mater. 10 (2020), 1903120, https://doi.org/10.1002/aenm.201903120.

[12] M. Wang, L. Zhang, Y. He, H. Zhu, Recent advances in transition-metal-sulfide-based bifunctional electrocatalysts for overall water splitting, J. Mater. Chem. A 9 (2021) 5320–5363, https://doi.org/10.1039/d0ta12152e.

[13] Y. Zhao, B. Jin, Y. Zheng, H. Jin, Y. Jiao, S.Z. Qiao, Charge state manipulation of cobalt selenide catalyst for overall seawater electrolysis, Adv. Energy Mater. 8 (2018), 1801926, https://doi.org/10.1002/AENM.201801926.

[14] X. Xia, L. Wang, N. Sui, V.L. Colvin, W.W. Yu, Recent progress in transition metal selenide electrocatalysts for water splitting, Nanoscale 12 (2020) 12249–12262, https://doi.org/10.1039/D0NR02939D.

[15] M.R. Gao, M.K.Y. Chan, Y. Sun, Edge-terminated molybdenum disulfide with a 9.4-Å interlayer spacing for electrochemical hydrogen production, Nat. Commun. 61 (6) (2015) 1–8, https://doi.org/10.1038/ncomms8493.

[16] Z. Zhuang, Q. Peng, J. Zhuang, X. Wang, Y. Li, Controlled hydrothermal synthesis and structural characterization of a nickel selenide series, Chem. Eur. J. 12 (2006) 211–217, https://doi.org/10.1002/CHEM.200500724.

[17] H. Zhou, F. Yu, Y. Liu, J. Sun, Z. Zhu, R. He, J. Bao, W.A. Goddard, S. Chen, Z. Ren, Outstanding hydrogen evolution reaction catalyzed by porous nickel diselenide electrocatalysts, Energy Environ. Sci. 10 (2017) 1487–1492, https://doi.org/10.1039/C7EE00802C.

[18] B. Lin, J. Chen, R. Yang, S. Mao, M. Qin, Y. Wang, Multi-hierarchical cobalt-based electrocatalyst towards high rate H2 production, Appl. Catal. B Environ. 316 (2022), 121666, https://doi.org/10.1016/J.APCATB.2022.121666.

[19] X. Wang, H. Zhou, D. Zhang, M. Pi, J. Feng, S. Chen, Mn-doped NiP2 nanosheets as an efficient electrocatalyst for enhanced hydrogen evolution reaction at all pH values, J. Power Sources 387 (2018) 1–8, https://doi.org/10.1016/J.JPOWSOUR.2018.03.053.

[20] M. Maleki, G.B. Darband, A.S. Rouhaghdam, R. Andaveh, Z.M. Kazemi, Mn-incorporated nickel selenide: an ultra-active bifunctional electrocatalyst for hydrogen evolution and urea oxidation reactions, Chem. Commun. 58 (2022) 3545–3548, https://doi.org/10.1039/D1CC07242K.

[21] P.E. Blöchl, Projector augmented-wave method, Phys. Rev. B 50 (1994) 17953, https://doi.org/10.1103/PhysRevB.50.17953.

[22] J.P. Perdew, K. Burke, M. Ernzerhof, Generalized gradient approximation made simple, Phys. Rev. Lett. 77 (1996) 3865, https://doi.org/10.1103/PhysRevLett.77.3865.

[23] S. Grimme, J. Antony, S. Ehrlich, H. Krieg, A consistent and accurate ab initio parametrization of density functional dispersion correction (DFT-D) for the 94 elements H-Pu, J. Chem. Phys. 132 (2010), 154104, https://doi.org/10.1063/1.3382344.

[24] Q. Fu, Y. Luo, Catalytic activity of single transition-metal atom doped in Cu(111) surface for heterogeneous hydrogenation, J. Phys. Chem. C 117 (2013) 14618–14624, https://doi.org/10.1021/JP403902G/ASSET/IMAGES/MEDIUM/JP-2013-03902G_0009.GIF.

[25] M. Qian, S. Cui, D. Jiang, L. Zhang, P. Du, Highly efficient and stable water-oxidation electrocatalysis with a very low overpotential using fenip substitutional-solid-solution nanoplate arrays, Adv. Mater. 29 (2017), 1704075, https://doi.org/10.1002/ADMA.201704075.

[26] B. Zhao, J. Liu, C. Xu, R. Feng, P. Sui, L. Wang, J. Zhang, J.L. Luo, X.Z. Fu, Hollow NiSe nanocrystals heterogenized with carbon nanotubes for efficient electrocatalytic methanol upgrading to boost hydrogen co-production, Adv. Funct. Mater. 31 (2021), 2008812, https://doi.org/10.1002/ADFM.202008812.

[27] P. Ganesan, A. Sivanantham, S. Shanmugam, Nanostructured nickel-cobalt-titanium alloy grown on titanium substrate as efficient electrocatalyst for alkaline water electrolysis, ACS Appl. Mater. Interfaces 9 (2017) 12416–12426, https://doi.org/10.1021/ACSAMI.7B00353/SUPPL_FILE/AM7B00353_SI_001.PDF.

[28] A. Panneerselvam, M.A. Malik, M. Afzaal, P. O'Brien, M. Helliwell, The chemical vapor deposition of nickel phosphide or selenide thin films from a single precursor, J. Am. Chem. Soc. 130 (2008) 2420–2421, https://doi.org/10.1021/JA078202J/SUPPL_FILE/JA078202J-FILE002.CIF.

[29] B. Zhao, J. Liu, C. Xu, R. Feng, P. Sui, L. Wang, J. Zhang, J.L. Luo, X.Z. Fu, Hollow NiSe nanocrystals heterogenized with carbon nanotubes for efficient electrocatalytic methanol upgrading to boost hydrogen co-production, Adv. Funct. Mater. 31 (2021), 2008812, https://doi.org/10.1002/ADFM.202008812.

[30] X. Xu, F. Song, X. Hu, A nickel iron diselenide-derived efficient oxygen-evolution catalyst, Nat. Commun. 71 (7) (2016) 1–7, https://doi.org/10.1038/ncomms12324.

[31] H. Dan, K. Tao, Y. Hai, L. Liu, Y. Gong, (Co, Mn)-Doped NiSe2-diethylenetriamine (dien) nanosheets and (Co, Mn, Sn)-doped NiSe2 nanowires for high performance supercapacitors: compositional/morphological evolution and (Co, Mn)-induced electron transfer, Nanoscale 11 (2019) 16810–16827, https://doi.org/10.1039/C9NR04478G.

[32] F. Wang, P. He, Y. Li, T.A. Shifa, Y. Deng, K. Liu, Q. Wang, F. Wang, Y. Wen, Z. Wang, X. Zhan, L. Sun, J. He, Interface engineered WxC@WS2 nanostructure for enhanced hydrogen evolution catalysis, Adv. Funct. Mater. 27 (2017), 1605802, https://doi.org/10.1002/ADFM.201605802.

[33] X. Cao, J. Wu, C. Jin, J. Tian, P. Strasser, R. Yang, MnCo2O4 anchored on P-doped hierarchical porous carbon as an electrocatalyst for high-performance rechargeable Li-O2 batteries, ACS Catal. 5 (2015) 4890–4896, https://doi.org/10.1021/ACSCATAL.5B00494/SUPPL_FILE/CS5B00494_SI_001.PDF.

[34] Z. Wang, Y. Hu, W. Liu, L. Xu, M. Guan, Y. Zhao, J. Bao, H. Li, Manganese-modulated cobalt-based layered double hydroxide grown on nickel foam with 1D–2D–3D heterostructure for highly efficient oxygen evolution reaction and urea oxidation reaction, Chem. Eur. J. 26 (2020) 9382–9388, https://doi.org/10.1002/CHEM.202001055.

[35] Y. Luo, L. Tang, U. Khan, Q. Yu, H.M. Cheng, X. Zou, B. Liu, Morphology and surface chemistry engineering toward pH-universal catalysts for hydrogen evolution at high current density, Nat. Commun. 101 (10) (2019) 1–9, https://doi.org/10.1038/s41467-018-07792-9.

[36] I.S. Kwon, I.H. Kwak, T.T. Debela, H.G. Abbas, Y.C. Park, J.P. Ahn, J. Park, H.S. Kang, Se-rich MoSe2 nanosheets and their superior electrocatalytic performance for hydrogen evolution reaction, ACS Nano 14 (2020) 6295–6304, https://doi.org/10.1021/ACSNANO.0C02593/SUPPL_FILE/NN0C02593_SI_001.PDF.

[37] Y. Yan, B.Y. Xia, B. Zhao, X. Wang, A review on noble-metal-free bifunctional heterogeneous catalysts for overall electrochemical water splitting, J. Mater. Chem. A 4 (2016) 17587–17603, https://doi.org/10.1039/C6TA08075H.

[38] Y. Liu, H. Jiang, Z. Hou, Hidden mechanism behind the roughness-enhanced selectivity of carbon monoxide electrocatalytic reduction, Angew. Chem. Int. Ed. 60 (2021) 11133–11137, https://doi.org/10.1002/ANIE.202016332.

[39] S. Anantharaj, S. Kundu, Do the evaluation parameters reflect intrinsic activity of electrocatalysts in electrochemical water splitting? ACS Energy Lett. 4 (2019) 1260–1264, https://doi.org/10.1021/ACSENERGYLETT.9B00686/ASSET/IMAGES/MEDIUM/NZ-2019-00686J_M003.GIF.

[40] M. Sadaqat, L. Nisar, N.U.A. Babar, F. Hussain, M.N. Ashiq, A. Shah, M.F. Ehsan, M. Najam-Ul-Haq, K.S. Joya, Zinc-telluride nanospheres as an efficient water oxidation electrocatalyst displaying a low overpotential for oxygen evolution, J. Mater. Chem. A 7 (2019) 26410–26420, https://doi.org/10.1039/C9TA07171G.

[41] Y. Luo, L. Tang, U. Khan, Q. Yu, H.M. Cheng, X. Zou, B. Liu, Morphology and surface chemistry engineering toward pH-universal catalysts for hydrogen

evolution at high current density, Nat. Commun. 101 (10) (2019) 1–9, https://doi.org/10.1038/s41467-018-07792-9.

[42] R. Andaveh, G.B. Darband, M. Maleki, A.S. Rouhaghdam, Superaerophobic/superhydrophilic surfaces as advanced electrocatalysts for the hydrogen evolution reaction: a comprehensive review, J. Mater. Chem. A 10 (2022) 5147–5173, https://doi.org/10.1039/D1TA10519A.

[43] K. Dastafkan, Q. Meyer, X. Chen, C. Zhao, Efficient oxygen evolution and gas bubble release achieved by a low gas bubble adhesive iron–nickel vanadate electrocatalyst, Small 16 (2020), 2002412, https://doi.org/10.1002/SMLL.202002412.

[44] M. Maleki, A. Sabour Rouhaghdam, G. Barati Darband, D. Han, S. Shanmugam, Highly active and durable NiCoSeP nanostructured electrocatalyst for large-current-density hydrogen production, ACS Appl. Energy Mater. (2021), https://doi.org/10.1021/ACSAEM.1C03625/SUPPL_FILE/AE1C03625_SI_003.PDF.

[45] Y. Li, X. Wei, L. Chen, J. Shi, M. He, Nickel-molybdenum nitride nanoplate electrocatalysts for concurrent electrolytic hydrogen and formate productions, Nat. Commun. 101 (10) (2019) 1–12, https://doi.org/10.1038/s41467-019-13375-z.

[46] L. Gao, Z. Liu, J. Ma, L. Zhong, Z. Song, J. Xu, S. Gan, D. Han, L. Niu, NiSe@NiOx core-shell nanowires as a non-precious electrocatalyst for upgrading 5-hydroxymethylfurfural into 2,5-furandicarboxylic acid, Appl. Catal. B Environ. 261 (2020), 118235, https://doi.org/10.1016/J.APCATB.2019.118235.

[47] C.B. Sun, M.W. Guo, S.S. Siwal, Q.B. Zhang, Efficient hydrogen production via urea electrolysis with cobalt doped nickel hydroxide-riched hybrid films: cobalt doping effect and mechanism aspect, J. Catal. 381 (2020) 454–461, https://doi.org/10.1016/J.JCAT.2019.11.034.

[48] Y. Luo, L. Tang, U. Khan, Q. Yu, H.M. Cheng, X. Zou, B. Liu, Morphology and surface chemistry engineering toward pH-universal catalysts for hydrogen evolution at high current density, Nat. Commun. 101 (10) (2019) 1–9, https://doi.org/10.1038/s41467-018-07792-9.

[49] X. Ge, Y. Liu, F.W.T. Goh, T.S.A. Hor, Y. Zong, P. Xiao, Z. Zhang, S.H. Lim, B. Li, X. Wang, Z. Liu, Dual-phase spinel MnCo2O4 and spinel MnCo 2O4/nanocarbon hybrids for electrocatalytic oxygen reduction and evolution, ACS Appl. Mater. Interfaces 6 (2014) 12684–12691, https://doi.org/10.1021/am502657c.

[50] C.E. Beall, E. Fabbri, T.J. Schmidt, Perovskite oxide based electrodes for the oxygen reduction and evolution reactions: the underlying mechanism, ACS Catal. 11 (2021) 3094–3114, https://doi.org/10.1021/ACSCATAL.0C04473/ASSET/IMAGES/LARGE/CS0C04473_0014.JPEG.

[51] D. Friebel, M.W. Louie, M. Bajdich, K.E. Sanwald, Y. Cai, A.M. Wise, M.J. Cheng, D. Sokaras, T.C. Weng, R. Alonso-Mori, R.C. Davis, J.R. Bargar, J.K. Nørskov, A. Nilsson, A.T. Bell, Identification of highly active Fe sites in (Ni,Fe)OOH for electrocatalytic water splitting, J. Am. Chem. Soc. 137 (2015) 1305–1313, https://doi.org/10.1021/JA511559D/SUPPL_FILE/JA511559D_SI_001.PDF.

[52] S. Hirai, S. Yagi, A. Seno, M. Fujioka, T. Ohno, T. Matsuda, Enhancement of the oxygen evolution reaction in Mn3+-based electrocatalysts: correlation between Jahn–Teller distortion and catalytic activity, RSC Adv. 6 (2015) 2019–2023, https://doi.org/10.1039/C5RA22873E.

[53] X. Ge, Y. Liu, F.W.T. Goh, T.S.A. Hor, Y. Zong, P. Xiao, Z. Zhang, S.H. Lim, B. Li, X. Wang, Z. Liu, Dual-phase spinel MnCo2O4 and spinel MnCo 2O4/nanocarbon hybrids for electrocatalytic oxygen reduction and evolution, ACS Appl. Mater. Interfaces 6 (2014) 12684–12691, https://doi.org/10.1021/AM502675C/SUPPL_FILE/AM502675C_SI_001.PDF.

[54] A. Bhargava, C.Y. Chen, K. Dhaka, Y. Yao, A. Nelson, K.D. Finkelstein, C.J. Pollock, M. Caspary Toroker, R.D. Robinson, Mn cations control electronic transport in spinel CoxMn3-xO4 nanoparticles, Chem. Mater. 31 (2019) 4228–4233, https://doi.org/10.1021/ACS.CHEMMATER.9B01198/SUPPL_FILE/CM9B01198_SI_001.PDF.

[55] X. Su, Y. Wang, J. Zhou, S. Gu, J. Li, S. Zhang, Operando spectroscopic identification of active sites in NiFe Prussian Blue analogues as electrocatalysts: activation of oxygen atoms for oxygen evolution reaction, J. Am. Chem. Soc. 140 (2018) 11286–11292, https://doi.org/10.1021/JACS.8B05294/SUPPL_FILE/JA8B05294_SI_001.PDF.

[56] C. Walter, S. Kalra, R. Beltrán-Suito, M. Schwarze, P.W. Menezes, M. Driess, Manganese sulfide enables the formation of a highly active β-MnOOH electrocatalyst for effective alkaline water oxidation, Mater. Today Chem. 24 (2022), 100905, https://doi.org/10.1016/J.MTCHEM.2022.100905.

[57] W. Hu, Q. Liu, T. Lv, F. Zhou, Y. Zhong, Impact of interfacial CoOOH on OER catalytic activities and electrochemical behaviors of bimetallic CoxNi-LDH nanosheet catalysts, Electrochim. Acta 381 (2021), 138276, https://doi.org/10.1016/J.ELECTACTA.2021.138276.

[58] J. Villalobos, D.M. Morales, D. Antipin, G. Schuck, R. Golnak, J. Xiao, M. Risch, Stabilization of a Mn−Co Oxide During Oxygen Evolution in Alkaline Media, ChemElectroChem 9 (2022), e202200482, https://doi.org/10.1002/CELC.202200482.

[59] T. Wu, S. Sun, J. Song, S. Xi, Y. Du, B. Chen, W.A. Sasangka, H. Liao, C.L. Gan, G.G. Scherer, L. Zeng, H. Wang, H. Li, A. Grimaud, Z.J. Xu, Iron-facilitated dynamic active-site generation on spinel CoAl2O4 with self-termination of surface reconstruction for water oxidation, Nat. Catal. 29 (2) (2019) 763–772, https://doi.org/10.1038/s41929-019-0325-4.

[60] T. Li, S. Li, Q. Liu, Y. Tian, Y. Zhang, G. Fu, Y. Tang, Hollow Co3O4/CeO2 heterostructures in situ embedded in N-doped carbon nanofibers enable outstanding oxygen evolution, ACS Sustain. Chem. Eng. 7 (2019) 17950–17957, https://doi.org/10.1021/ACSSUSCHEMENG.9B04699/SUPPL_FILE/SC9B04699_SI_001.PDF.

[61] Q. Hu, K. Gao, X. Wang, H. Zheng, J. Cao, L. Mi, Q. Huo, H. Yang, J. Liu, C. He, Subnanometric Ru clusters with upshifted D band center improve performance for alkaline hydrogen evolution reaction, Nat. Commun. 131 (13) (2022) 1–10, https://doi.org/10.1038/s41467-022-31660-2.

[62] L. Zhang, M. Hu, H. Li, B. Cao, P. Jing, B. Liu, R. Gao, J. Zhang, B. Liu, Boosting hydrogen evolution reaction via electronic coupling of cerium phosphate with molybdenum phosphide nanobelts, Small 17 (2021), 2102413, https://doi.org/10.1002/SMLL.202102413.

[63] H. Zhou, F. Yu, Y. Huang, J. Sun, Z. Zhu, R.J. Nielsen, R. He, J. Bao, W.A. Goddard, S. Chen, Z. Ren, Efficient hydrogen evolution by ternary molybdenum sulfoselenide particles on self-standing porous nickel diselenide foam, Nat. Commun. 7 (2016) 1–7, https://doi.org/10.1038/ncomms12765.

[64] L. Cao, Q. Luo, J. Chen, L. Wang, Y. Lin, H. Wang, X. Liu, X. Shen, W. Zhang, W. Liu, Z. Qi, Z. Jiang, J. Yang, T. Yao, Dynamic oxygen adsorption on single-atomic Ruthenium catalyst with high performance for acidic oxygen evolution reaction, Nat. Commun. 10 (2019) 4849, https://doi.org/10.1038/s41467-019-12886-z.

[65] B. Zhang, Z. Du, R. Sun, X. Lai, J. Lan, X. Liu, L. Yan, Tremella-like Ni–NiO with O-vacancy heterostructure nanosheets grown in situ on MXenes for highly efficient hydrogen and oxygen evolution, ACS Appl. Mater. Interfaces 14 (2022) 47529–47541, https://doi.org/10.1021/acsami.2c10482.

[66] X.Y. Yu, Y. Feng, B. Guan, X.W.D. Lou, U. Paik, Carbon coated porous nickel phosphides nanoplates for highly efficient oxygen evolution reaction, Energy Environ. Sci. 9 (2016) 1246–1250, https://doi.org/10.1039/C6EE00100A.